Future Changes in African Heatwaves and Their Drivers at the Convective Scale

C. E. BIRCH,[a] L. S. JACKSON,[a] D. L. FINNEY,[a,b] J. M. MARSHAM,[c] R. A. STRATTON,[d] S. TUCKER,[d] S. CHAPMAN,[a]
C. A. SENIOR,[d] R. J. KEANE,[a,d] F. GUICHARD,[e] AND E. J. KENDON[d]

[a] *School of Earth and Environment, University of Leeds, Leeds, United Kingdom*
[b] *Ronin Institute for Independent Scholarship, Montclair, New Jersey*
[c] *University of Leeds Met Office Strategic (LUMOS) Research Group, School of Earth and Environment, University of Leeds, Leeds, United Kingdom*
[d] *Met Office, Exeter, United Kingdom*
[e] *CNRM, Université de Toulouse, Météo-France, CNRS, Toulouse, France*

(Manuscript received 14 October 2021, in final form 9 February 2022)

ABSTRACT: The future change in dry and humid heatwaves is assessed in 10-yr pan-African convective-scale (4.5 km) and parameterized convection (25 km) climate model simulations. Compared to reanalysis, the convective-scale simulation is better able to represent humid heatwaves than the parameterized simulation. Model performance for dry heatwaves is much more similar. Both model configurations simulate large increases in the intensity, duration, and frequency of heatwaves by 2100 under RCP8.5. Present-day conditions that occur on 3–6 heatwave days per year will be normal by 2100, occurring on 150–180 days per year. The future change in dry heatwaves is similar in both climate model configurations, whereas the future change in humid heatwaves is 56% higher in intensity and 20% higher in frequency in the convective-scale model. Dry heatwaves are associated with low rainfall, reduced cloud, increased surface shortwave heating, and increased sensible heat flux. In contrast, humid heatwaves are predominately controlled by increased humidity, rainfall, cloud, longwave heating, and evaporation, with dry-bulb temperature gaining more significance in the most humid regions. Approximately one-third (32%) of humid heatwaves commence on wet days. Moist processes are known to be better represented in convective-scale models. Climate models with parameterized convection, such as those in CMIP, may underestimate the future change in humid heatwaves, which heightens the need for mitigation and adaptation strategies and indicates there may be less time available to implement them to avoid future catastrophic heat stress conditions than previously thought.

SIGNIFICANCE STATEMENT: Temperatures are higher in dry heatwaves, but humid heatwaves can be more dangerous, as the ability to cool by sweating is limited. We found that dry heatwaves are caused by decreased cloud, allowing the sun to heat the surface, whereas humid heatwaves are caused by increased cloud, rainfall, and evaporation from the surface. We found that a state-of-the-art very high-resolution climate model predicts a larger future change in humid heatwaves compared to a more traditional global climate model. Previous estimates of the prevalence of humid heatwaves in the future may therefore be underestimated. If we do not cut emissions of greenhouse gases, present-day African heatwave conditions could be experienced on up to half of all days of the year by 2100.

KEYWORDS: Africa; Extreme events; Climate change; Convective-scale processes; Climate models

1. Introduction

There is mounting evidence that heatwaves, regardless of definition, have increased in intensity, frequency, and duration over Africa over the last three decades (Ceccherini et al. 2017; Fontaine et al. 2013; Lyon 2009; Moron et al. 2016; Seneviratne et al. 2021). The IPCC Working Group 1 Sixth Assessment Report (Seneviratne et al. 2021) states that at the continental scale, it is "very likely" the intensity and frequency of African hot extremes will increase even under 1.5°C global warming, and the changes are "virtually certain" to occur under 4°C global warming (Dosio 2017; Fitzpatrick et al. 2020a; Perkins-Kirkpatrick; Lewis 2020; Russo et al. 2016). Vicedo-Cabrera et al. (2021) attribute more than 40% of heat-related mortality in South Africa during the period 1991–2018 to human-induced climate change.

Humid heatwaves are extreme heat events that involve increases in both temperature and humidity. Humidity limits the body's ability to sweat and therefore plays a major role in heat stress (i.e., when the body's ability to control its internal temperature starts to fail; Kjellstrom et al. 2016). Equatorial Africa, in particular, is projected to be a global hotspot for heat stress by the end of the century (Coffel et al. 2017; Dosio et al. 2018; Mora et al. 2017). The impacts of heat stress in Africa—including deaths—go largely unreported (Harrington and Otto 2020) and the sparse observation network means humid temperature extremes in particular are hard to detect. Despite this, a small number of studies have shown that heatwaves cause harm in Africa (Azongo et al. 2012; Diboulo et al. 2012).

Supplemental information related to this paper is available at the Journals Online website: https://doi.org/10.1175/JCLI-D-21-0790.s1.

Author Guichard is deceased.

Corresponding author: Cathryn Birch, c.e.birch@leeds.ac.uk

DOI: 10.1175/JCLI-D-21-0790.1

There is limited literature on the drivers of humid heatwaves anywhere in the world (Raymond et al. 2021) and the vast majority of research on African heatwave drivers is focused on dry-bulb heatwaves in the Sahel region of sub-Saharan Africa. Dry-bulb temperature extremes in the Sahel due to moisture advection and surface longwave heating through the water vapor greenhouse gas effect have been highlighted in a number of studies (Fontaine et al. 2013; Guigma et al. 2020; Guigma et al. 2021; Largeron et al. 2020; Oueslati et al. 2017). Bouniol et al. (2021) analyzed daily maximum (daytime) and minimum (nighttime) dry-bulb temperature heatwaves over the Sahel using satellite-derived cloud, aerosol, water vapor, and radiative fluxes. They found that daytime heatwaves occur during reduced cloud, a lower aerosol load, and increased surface shortwave radiation flux. Conversely, nighttime heatwaves occur during periods with increased cloud, aerosol, and water vapor and a resulting increase in longwave heating that exceeds the decrease in shortwave heating.

Even within the discipline of meteorology, there is no universally accepted metric for dry or humid heatwaves and different metrics do not necessarily identify the same events (Guigma et al. 2020). A number of recent global studies have focused on metrics that account for both temperature and humidity because both are physiologically important for human heat stress (Coffel et al. 2017; Mora et al. 2017; Russo et al. 2017). Globally, 74% of the world's population is projected to be exposed to deadly heat stress for at least 20 days per year by 2100 under RCP8.5 (Mora et al. 2017). South Asian wet-bulb temperature is projected to approach, and in a few locations exceed, the critical threshold of 35°C, which is considered the limit of human survivability, by 2100 under high emission scenarios (Im et al. 2017; Pal and Eltahir 2016).

Projections of future heat extremes are almost ubiquitously provided by relatively coarse-resolution regional (Gutowski et al. 2016) or global climate (Eyring et al. 2016; Taylor et al. 2012) models, which require a parameterization scheme to represent convective rainfall processes. Such models are known to poorly represent tropical rainfall characteristics, whereas convective-scale climate models are better able to represent intense rainfall and dry spells (Berthou et al. 2019b; Finney et al. 2020; Prein et al. 2015), related processes such as storm life cycles and propagation (Crook et al. 2019; Finney et al. 2020), the atmospheric overturning circulation (Hart et al. 2018; Jackson et al. 2020), the atmospheric water cycle (Birch et al. 2014b; Finney et al. 2019), and soil moisture–precipitation feedbacks (Taylor et al. 2013). Additionally, they project larger future increases in rainfall extremes (Berthou et al. 2019a; Finney et al. 2020; Kendon et al. 2014, 2019). Emerging studies suggest that heat extremes over Europe are better represented and the increases under climate change are larger in magnitude in convective-scale climate models (Kennedy-Asser et al. 2020; Tölle et al. 2018). It is not currently known if African heat extremes are better represented in convective-scale models, although given the crucial role of convection in African weather, the representation of convection is likely to be important. It is, therefore, critical to understand how African heatwave projections from global models are affected by their parameterization of convection.

This study uses 10-yr pan-African climate simulations with 4.5-km (convective scale) and 25-km (convection parameterized) horizontal grid spacing (Senior et al. 2021; Stratton et al. 2018). We evaluate the present-day mean temperature and humidity in the climate models using observations and reanalysis (section 3a). We assess the present-day values and future changes (2100, RCP8.5) in the intensity, duration, and frequency of wet- and dry-bulb heatwaves in the climate model simulations (section 3b). We demonstrate the contrasting drivers of wet- and dry-bulb heatwaves over Africa (section 3c) and show how the drivers of humid heatwaves differ over different regions of Africa (section 3d). We explain why the convective-scale climate model simulates a larger number of more intense and longer duration heatwaves under climate change than the climate model with parameterized convection (section 3d).

2. Data and methods

a. Model simulations

This study utilizes two 10-yr regional atmosphere-only climate simulations using the Met Office Unified Model (MetUM) run over a pan-Africa domain of 25°W–57°E, 45°S–40°N (Stratton et al. 2018). Both simulations are driven by the N512 (approximately 25 km × 40 km in the tropics) global atmosphere-only (GA7) configuration of the MetUM (Walters et al. 2017). The first regional model (CP4) has a horizontal grid spacing at the equator of 4.5 km × 4.5 km (0.04° × 0.04°) and is "convective-scale" (i.e., its horizontal resolution is sufficient to not require a parameterization for convection and it is switched off). The second regional model (P25) has a horizontal grid spacing matching the global model and includes parameterized convection (Gregory and Rowntree 1990; Walters et al. 2017). P25 is also based on the GA7 configuration, but to restrict differences between P25 and CP4 to convection some settings such as soil types and aerosol forcing have been made the same as those in CP4.

In the historical period, representing the years 1997–2006, all models use Reynolds daily sea surface temperature (SST) observations (Reynolds et al. 2007; Stratton et al. 2018). The future climate simulations use the representative concentration pathway (RCP) 8.5 for greenhouse gas concentrations for the year 2100 (Moss et al. 2010). In all the future simulations (CP4FUT, P25FUT, and the driving GCM) the average SST change between 1975–2005 and 2085–2115 in a separate CMIP5 HadGEM2-ES RCP8.5 run is added to the historical SSTs (Kendon et al. 2019).

The CP4 data were interpolated onto the P25 grid, and all subsequent analysis is performed on the P25 grid. Regridding the P25 and CP4 data onto a much coarser grid of 2° × 2° made negligible difference to the results (not shown). The full 10 years of simulation data, from January 1997 to December 2006, were used. Dropping the first year to allow for spinup made negligible difference to all results (not shown).

b. Observations and reanalysis

We diagnose dry-bulb heatwaves using near-surface daily maximum temperature ($T_{\max}$) observations from the Berkeley Earth

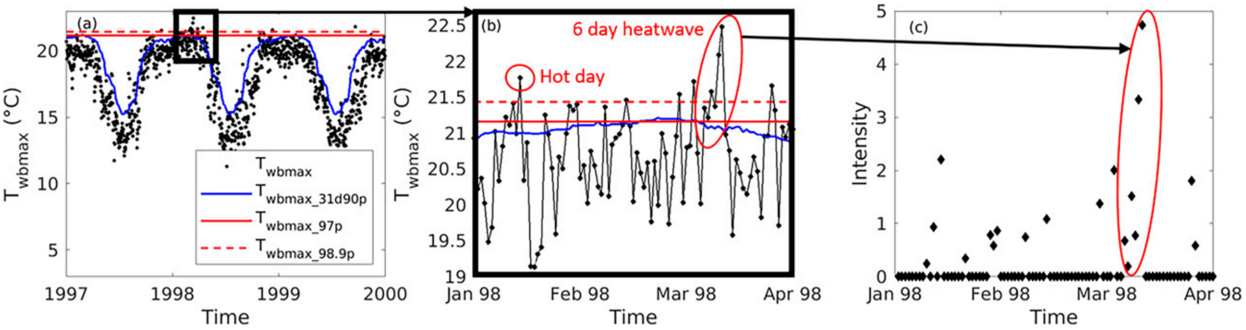

FIG. 1. (a) Illustration of the heatwave identification method for one arbitrary grid box in CP4, with (b),(c) consecutively zoomed in views of (a). The black dots represent daily T_{wbmax} over an example 3-yr time slice. The blue line is the 90th percentile of T_{wbmax} over a 31-day running window. The red solid and dashed lines are the 97th and 98.9th percentiles, respectively, of T_{wbmax} over all days and all years. The dots in (c) show the unitless heat intensity on each identified hot day.

Surface Temperature gridded dataset (BEST). It uses the statistical kriging method to interpolate data from weather stations compiled from a number of data archives onto a global regular 1° × 1° grid (Rohde and Hausfather 2020). We evaluate the mean temperature in the climate models using monthly mean near-surface temperature from the Climatic Research Unit (CRU) TS4.03 reference dataset, on a 0.5° × 0.5° grid (Harris et al. 2020).

We diagnose both wet- and dry-bulb heatwaves using hourly data from the fifth generation of the European reanalysis (ERA5) at the native horizontal resolution of 0.25° × 0.25° (~30 km) (Hersbach et al. 2020). We note that ERA5 is produced by an atmospheric model, itself with parameterized convection. It cannot be considered as "observations" and the drivers of the heatwaves in ERA5 may suffer from similar biases as the climate models, particularly P25. Previous work has compared and evaluated daily maximum and minimum dry-bulb temperature in four reanalysis products, including ERA-Interim, the ERA5 predecessor, against the BEST dataset and found that ERA-Interim performed the best (Barbier et al. 2018). There are limitations in using reanalysis datasets but there are also likely big uncertainties in the BEST and CRU datasets due to the sparsity of surface station observations over Africa.

To evaluate the diurnal cycles of dry- and wet-bulb temperature and humidity in reanalysis and the climate model simulations, we use hourly observations from three weather stations, with multiyear subhourly records that include humidity. The stations are located in Skukuza, South Africa (25.0°S, 31.5°E), which has data available for 2000–13 (Pastorello et al. 2020); Demokeya, Kordofan, central Sudan (13.3°N, 30.5°E), which has data available for 2002–12 (Ardö 2013); and Banizoumbou, Niamey, Niger (13.5°N, 2.7°E), where data for 2008–15 were used (Lebel et al. 2009).

We use the daily Integrated Multi-satellitE Retrievals for GPM (IMERG) satellite retrievals of rainfall (Huffman et al. 2014), available from mid-2000 to near-present. The IMERG data are interpolated onto the ERA5 grid before any analysis is performed.

c. *Heatwave identification*

Heatwaves are defined using near-surface daily maximum dry (T_{max}) or wet (T_{wbmax}) bulb temperature over the pan-Africa region of 22°W–54°E, 42°S–37°N, which includes the Arabian Peninsula, for land points only. This means a 3° band around the edge of the model domains has been removed to allow for the effects of the lateral boundary conditions. There are various quantities that can be used to represent humidity in heat stress, including wet-bulb temperature, wet-bulb globe temperature, and apparent temperature. Sherwood (2018) shows that although all three of these quantities increase with increasing humidity, wet-bulb temperature is the most sensitive to humidity, which makes it a good choice here in order to best highlight the differences in the drivers of T_{max} and T_{wbmax} heatwaves.

Hourly wet-bulb temperature is computed from hourly specific humidity, dry-bulb temperature, and pressure using the method of Davies-Jones (2008) and then the daily maximum, T_{wbmax}, is found. The results are not sensitive to using hourly dry-bulb temperature to compute T_{max}, rather than the daily dry-bulb maximum temperature output directly from the model simulations. Because T_{wbmax} was not output directly from the climate model simulations, it was necessary to compute the daily maximums from the hourly data because, due to the diurnal cycle of humidity, it is essential to use hourly rather than daily mean humidity data to compute T_{wbmax} (see section 2d). For consistency, we also use hourly data to calculate T_{max}.

Heatwaves were identified as follows (described here for T_{wbmax} heatwaves; a description of the differences between how T_{wbmax} and T_{max} heatwaves are diagnosed follows):

1) For each grid box, the 90th percentile of T_{wbmax} over a 31-day running window, T_{wbmax_31d90p} (blue line, Fig. 1) and the 97th percentile of daily maximum wet-bulb temperature over all days in the dataset, T_{wbmax_97p} (red solid line, Fig. 1) are computed.
2) Hot days are defined as days where T_{wbmax} (black dots, Fig. 1) are above both the blue and red solid lines (i.e., unseasonably warm days in the colder months are not diagnosed as hot days).
3) A heatwave event is defined as 3 or more consecutive hot days. A "heatwave day" is defined as each individual day within a heatwave event.

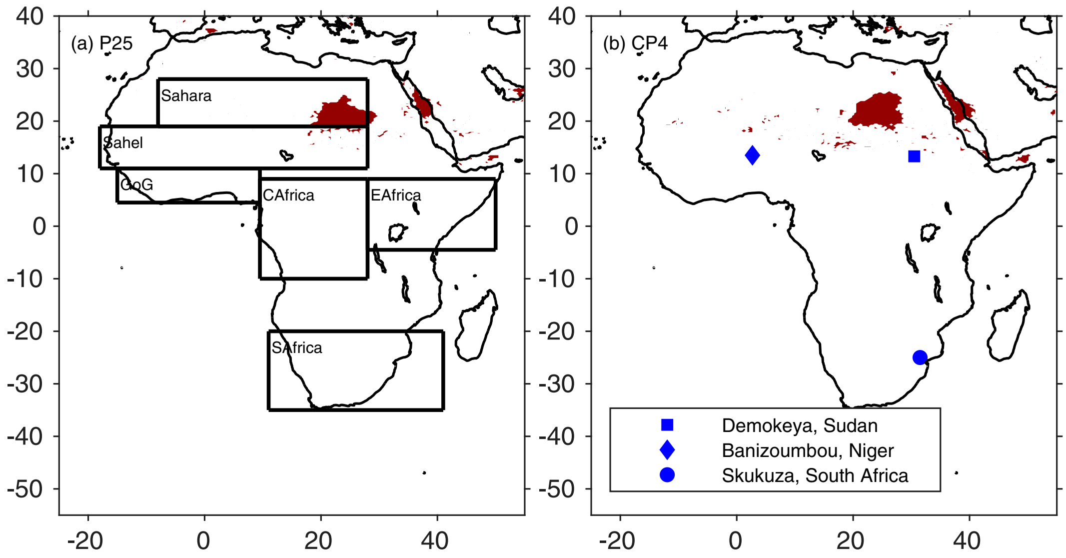

FIG. 2. Example heatwave on 25 Jun 2001 in P25 and CP4. The grid boxes where a heatwave was identified on this day are marked in red. Also shown are the subregions used later in the analysis and the locations of the three weather stations used in Fig. 3. GoG = Gulf of Guinea.

Three key metrics are recorded for each grid box: the duration of each heatwave, the intensity of each heatwave day (defined below), and the total number of heatwave days that occur over the length of the dataset (i.e., the frequency). The total number of heatwave days is analyzed, rather than the number of heatwave events, because the future change in heatwaves in the climate models is so large that most days in the future are diagnosed as heatwaves, so the number of events can decrease while the number of heatwaves days increases, and thus analyzing the number of heatwave events (and the heatwave duration) is misleading.

The intensity of each heatwave day is computed using a modified version of Eq. (2) in Russo et al. (2015):

$$I = \frac{T_{\mathrm{wbmax}} - T_{\mathrm{wbmax\_97p}}}{T_{\mathrm{wbmax\_98.9p}} - T_{\mathrm{wbmax\_97p}}},$$

where $T_{\mathrm{wbmax\_98.9p}}$ is the 98.9th percentile of daily maximum wet-bulb temperature over all days in the dataset (red dashed line, Fig. 1); I is a dimensionless measure of the intensity of each heatwave day relative to the variability of the hottest days that occur in each grid box.

This heatwave methodology was chosen because 1) it is a percentile-based metric, which allows ERA5 and the climate models to be directly compared regardless of differences in their mean climatology of temperature and humidity; 2) it is computed for each grid box separately, which allows the widely varying climates in Africa to be directly compared; and 3) it is possible to look at the intensity, duration, and frequency of heatwaves as separate metrics.

Heatwaves in CP4FUT and P25FUT are computed twice: once relative to the present-day baseline (i.e., $T_{\mathrm{wbmax\_31d90p}}$, $T_{\mathrm{wbmax\_97}}$, and $T_{\mathrm{wbmax\_98.9p}}$ are taken from the present-day simulation at each grid box) and once relative to the future climate baseline (i.e., $T_{\mathrm{wbmax\_31d90p}}$, $T_{\mathrm{wbmax\_97}}$, and $T_{\mathrm{wbmax\_98.9p}}$ are taken from the future climate simulation at each grid box). Heatwaves computed using the present-day baseline are used throughout the paper (except in Figs. 13, 15, and 16, where the future change in heatwave drivers is assessed). Future heatwaves are so frequent and long in duration under climate change that identifiable individual heatwaves do not exist in the future. Therefore, using the future climate baseline diagnoses a similar number of discrete heatwaves as are diagnosed in the present day.

Dry-bulb heatwaves are computed in the same way as above, by replacing T_{wbmax} with T_{max}. The only other difference is that the two percentile thresholds (red solid and dashed lines in Fig. 1) are set at $T_{\mathrm{max\_98}}$ and $T_{\mathrm{max\_99.9p}}$ for dry-bulb heatwaves, rather than the 97th and 98.9th percentile used for T_{max}. There is no clear choice of percentile in the literature, with different authors choosing to use different values (Guigma et al. 2020; Lyon 2009; Raymond et al. 2021; Russo et al. 2015). The consequence of using different percentiles for T_{max} and T_{wbmax} heatwaves is that the values of intensity are not directly comparable. However, it is done to make the number of T_{max} and T_{wbmax} heatwaves diagnosed in the present day similar, to provide consistency for the heatwave driver analysis.

For ERA5 we use two periods: 1) 1997–2006 for comparison of the ERA5 heatwave metrics with the present-day climate simulations and 2) 2000–19 when looking at atmospheric heatwave drivers, in order to align with the availability of the GPM rainfall observations. We compared with the period 1987–2016 to assess the impact of using a longer time series on the heatwave metrics. The mean and standard error of the pan-African heatwave metrics in ERA5 over 1997–2006, 1987–2016, and 2001–19 are as follows: for intensity, 1.36 ± 0.002, 1.41 ± 0.002, and 1.50 ± 0.002; for duration, 3.93 ± 0.003, 4.01 ± 0.002, and 3.97 ± 0.002 days; and for frequency, 2.5 ± 0.05, 2.7 ± 0.16, and

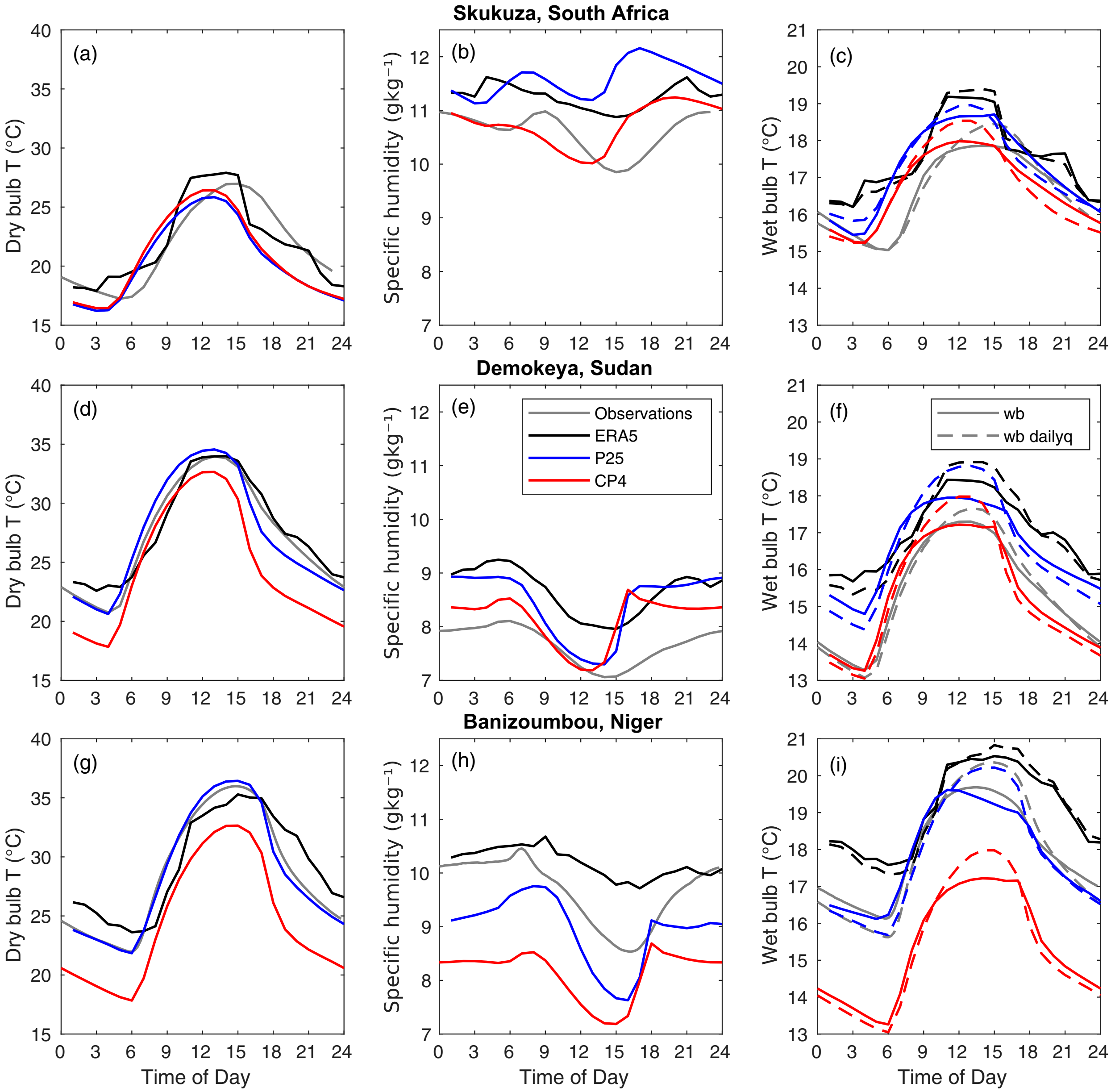

FIG. 3. Mean diurnal cycle of (left) near-surface dry bulb temperature, (center) near-surface specific humidity, and (right) wet bulb temperature at the locations of the surface stations in (a)–(c) South Africa, (d)–(f) Sudan, and (g)–(i) Niger. Wet-bulb temperature is computed using both hourly and daily mean q. Using daily mean or hourly surface pressure has negligible impact on the wet-bulb calculation. The locations of the three stations are illustrated in Fig. 2.

2.5 ± 0.10 days per year, respectively. These are negligible differences apart from in intensity, where a small climate change signal of higher intensity in later years is apparent, consistent with previous studies (Ceccherini et al. 2017). The relative importance of the different heatwave drivers is not dependent on the period used (not shown).

Figure 2 illustrates the resulting T_{wbmax} heatwave diagnosis in P25 and CP4 for an example day. The methodology is able to identify large, spatially coherent heatwaves. The event of 25 June 2001 is more than 4 years into the climate simulation, so the fact that both climate models produce a heatwave of a similar size and location at the same time suggests that the lateral boundary conditions and SSTs (which are the same in both simulations) have a strong control on this event.

d. Daily versus hourly specific humidity values in T_{wbmax} calculation

The mean diurnal cycle of near-surface specific humidity and wet- and dry-bulb temperature from ERA5, P25, and CP4 are plotted against observations from the three automatic weather stations (Fig. 3). Specific humidity has a diurnal cycle that is out of phase with the diurnal cycle in dry-bulb temperature at both

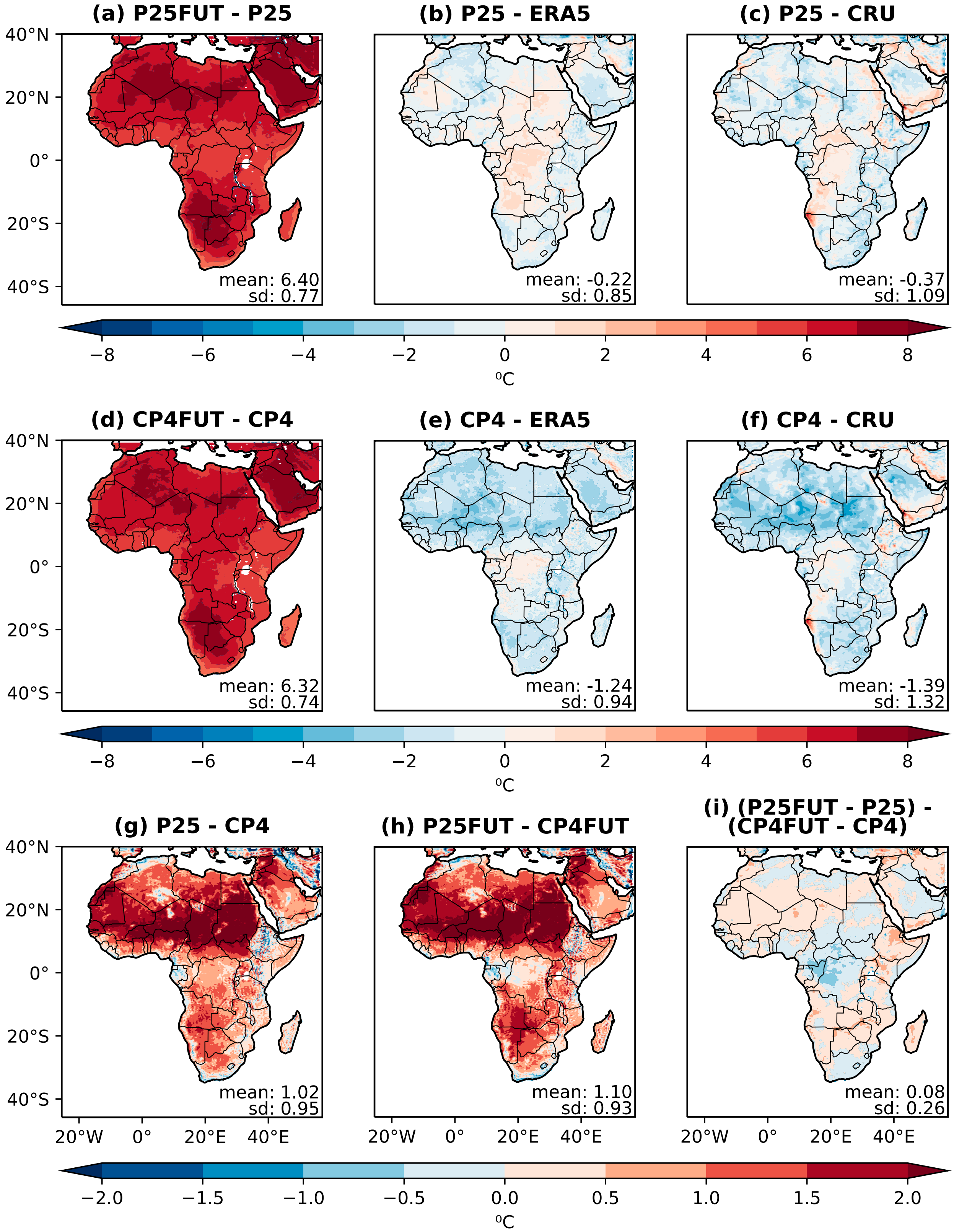

FIG. 4. Mean near-surface dry-bulb temperature. (a),(d) mean future changes, (b),(e) difference between present-day model simulations and ERA5, (c),(f) difference between present-day model simulations and CRU, and (g)–(i) differences between P25 and CP4 in the present day, future, and the future change.

locations, which is consistent with dry-air entrainment into the boundary layer during the day and moisture advection at night (Couvreux et al. 2015). This has a strong control on the magnitude and timing of T_{wbmax}, causing a flattening of the diurnal peak of wet-bulb temperature (solid lines, Figs. 3c,f,i).

Due to the lack of availability of subdaily humidity diagnostics from ensemble model studies such as CMIP5 (Taylor et al. 2012), CMIP6 (Eyring et al. 2016), and CORDEX (Gutowski et al. 2016), past studies that diagnose humid heatwaves using the daily maximum wet-bulb temperature [or wet-bulb globe temperature (WBGT)] (e.g., Russo et al. 2017; Coffel et al. 2017) necessarily use the daily mean, minimum, or maximum humidity to compute daily maximum humid-heat metrics. Using daily mean specific humidity in the calculation of T_{wbmax} produces a smooth diurnal cycle in wet-bulb temperature, which follows the shape of the diurnal cycle of dry-bulb temperature (dashed lines, Figs. 3c,f,i). The impact of the choice of daily or subdaily specific humidity on the present-day heatwave metrics used in this study is strikingly large and perhaps unpredictable, with no clear trend in the direction of the impact in ERA5, CP4, and P25 (see Fig. S1 in the online supplemental material). The future change in wet-bulb heatwave intensity, duration and frequency are overestimated in both CP4 (by 106%, 40%, and 16%, respectively) and P25 (by 73%, 16%, and 3%, respectively) when daily specific humidity is used in the T_{wbmax} calculation (Fig. S1). This is particularly important for wet-bulb temperature, which is the most sensitive to humidity out of the most frequently used humidity–temperature indices (Sherwood 2018).

e. *Computation of anomalies and climatologies*

Data shown in later figures (see Figs. 10, 14, 15, and 16) are presented as mean anomalies relative to a locally and temporally relevant climatology. For each heatwave diagnosed in ERA5 and the model simulations, a daily mean time series of each variable is extracted for a 31-day period, from day −15 to day 15, where day 0 is the onset of the heatwave. The local (i.e., grid box specific) daily mean annual cycle (31 values), smoothed using a 50-day running window, is subtracted from each 31-day time series to produce anomalies from the mean climatology at the relevant time of year. The bars (shown in Figs. 10, 14, 15, and 16) are an average of each anomaly over the first 3 days of all diagnosed heatwaves, so that each heatwave is weighted equally in the analysis. The exception is the humidity and temperature advection (q_{adv}, T_{adv}) (shown in Figs. 10 and 14), which are presented as absolute values for ease of interpretation.

f. *Statistical testing of rainfall distribution*

The Wilcoxon matched-pairs signed rank test is used to assess whether the distribution of daily rainfall accumulations on heatwave days is statistically significantly different ($p < 0.01$) to the climatological distribution of rainfall. For each heatwave, taking day −5 to day 5 in turn (where the first day of the heatwave is day 0), the difference between the rainfall accumulation on day x and the rainfall accumulation on day −15 is computed. It is assumed that day −15 is far enough away in time from the heatwave event to be sufficiently independent. The Wilcoxon signed rank test is performed 10 000 times on 1000 randomly selected difference pairs for each day from day −5 to day 5. This process is then repeated using daily rainfall accumulation on day 15, to allow for seasonal changes in rainfall between day −15 and day 15, which can be large around the time of monsoon onset.

The Wilcoxon matched-pairs signed rank test determines whether two dependent samples were selected from populations having the same distribution (i.e., the null hypothesis is that the medians of the heatwave and climatological rainfall are equal). It is an appropriate test because rainfall data do not have a normal distribution; instead, there are many more dry and/or low rainfall days than wet days.

3. Results

a. *Annual mean temperature and humidity*

An assessment of the mean dry-bulb temperature shows that there is a cold bias of 1.24° and 1.39°C in mean near-surface dry-bulb temperature in CP4 compared to ERA5 and CRU, respectively (Figs. 4e and 4f). P25 is also biased cold, but only by 0.22° and 0.37°C, respectively (Figs. 4b and 4c). In both the present-day and future climate, CP4 is on average ~1°C cooler than P25 (Figs. 4g and 4h). CP4 and P25 simulate future mean temperature increases by 2100 of 6.3° and 6.4°C, respectively (Figs. 4a and 4d), with P25 projecting a smaller increase in central Africa and CP4 predominately projecting a smaller increase elsewhere (Fig. 3i).

Compared to ERA5, CP4 and P25 have a mean dry bias of 0.88 and 0.50 g kg^{-1} in specific humidity, respectively, although P25 is wetter by 1–2 g kg^{-1} over central Africa (Figs. 5b and 5d). Both CP4 and P25 project mean future increases in specific humidity of ~3.4 g kg^{-1} (Figs. 5a and 5c) but the future change is ~1.5 g kg^{-1} larger in P25 over central Africa and ~0.5 g kg^{-1} larger in CP4 elsewhere (Fig. 5g). The resulting impact on mean wet-bulb temperature is a cold bias relative to ERA5 of 1.1° and 0.5°C in CP4 and P25, respectively (Figs. 6b and 6d), although the humidity bias in P25 in central Africa produces a warm bias in wet-bulb temperature of 0.5°–1°C. P25 is on average 0.6°–0.7°C warmer than CP4 in wet-bulb temperature in both the present day and future, with a large region of central Africa being up to 2°C warmer (Figs. 6e and 6f). The future change in mean wet-bulb temperature is ~4.4°C in both CP4 and P25 (Figs. 6a and 6c), with spatially variable differences in the future change between P25 and CP4 that are fairly small due to the compensating effects of humidity and temperature biases in the calculation of wet-bulb temperature (Fig. 6g). The cold and dry biases are consistent with those in other climate models (Fischer and Knutti 2013; Zhao et al. 2015).

b. *Wet- and dry-bulb heatwave metrics*

Summaries of present-day and future change in intensity, duration, and frequency of T_{wbmax} and $T_{\max}$ heatwaves in ERA5, P25, and CP4 (and BEST for $T_{\max}$) are shown in Fig. 7. For $T_{\max}$ intensity, there is relatively good agreement between ERA5, BEST, and both climate models (Fig. 7g). For T_{wbmax} intensity, both CP4 and P25 are skewed toward intensities < 1, although CP4 is much less so and is,

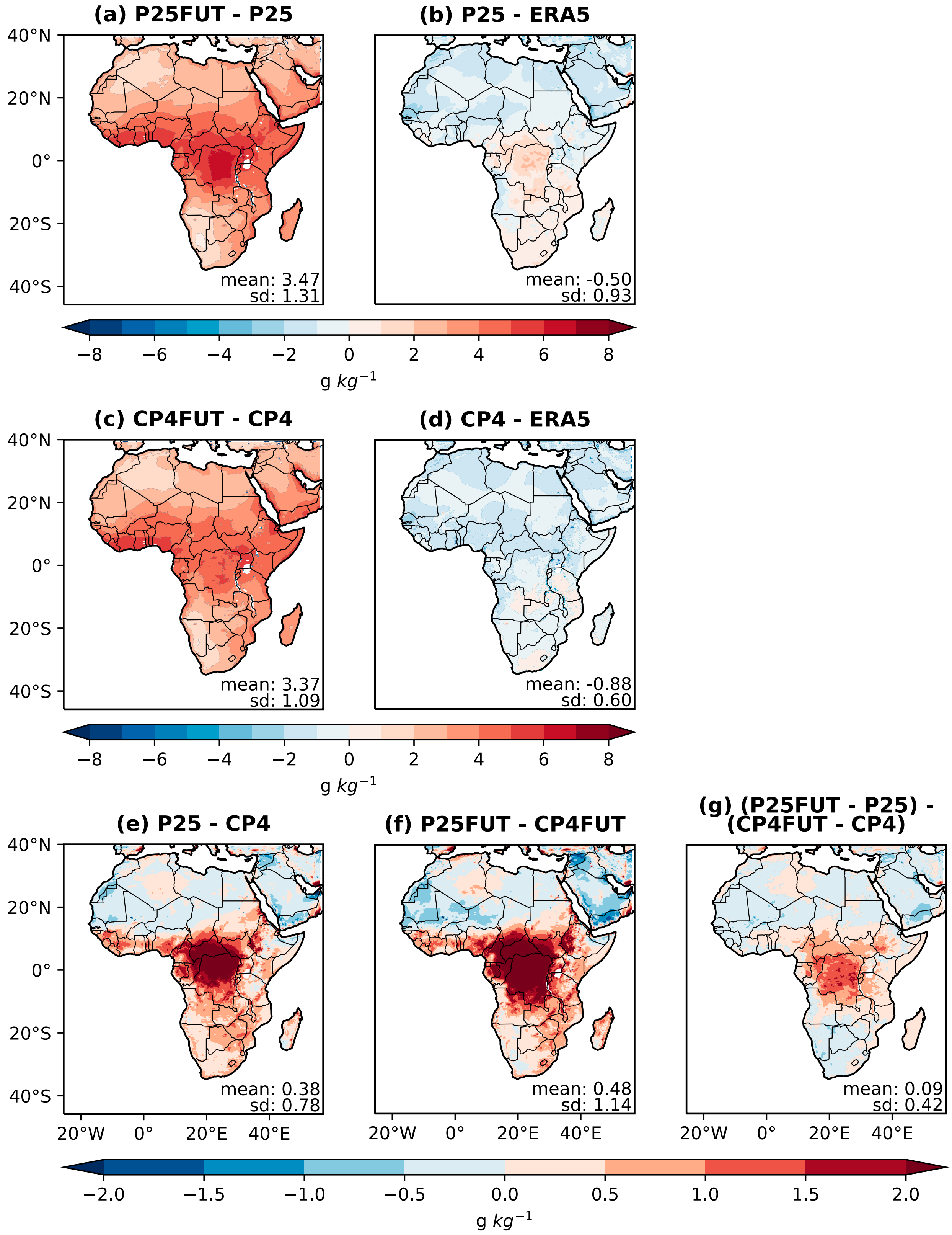

FIG. 5. Mean near-surface specific humidity: (a),(d) mean future changes, (b),(d) difference between present-day model simulations and ERA5, and (e)–(g) differences between P25 and CP4 in the present day, future, and the future change.

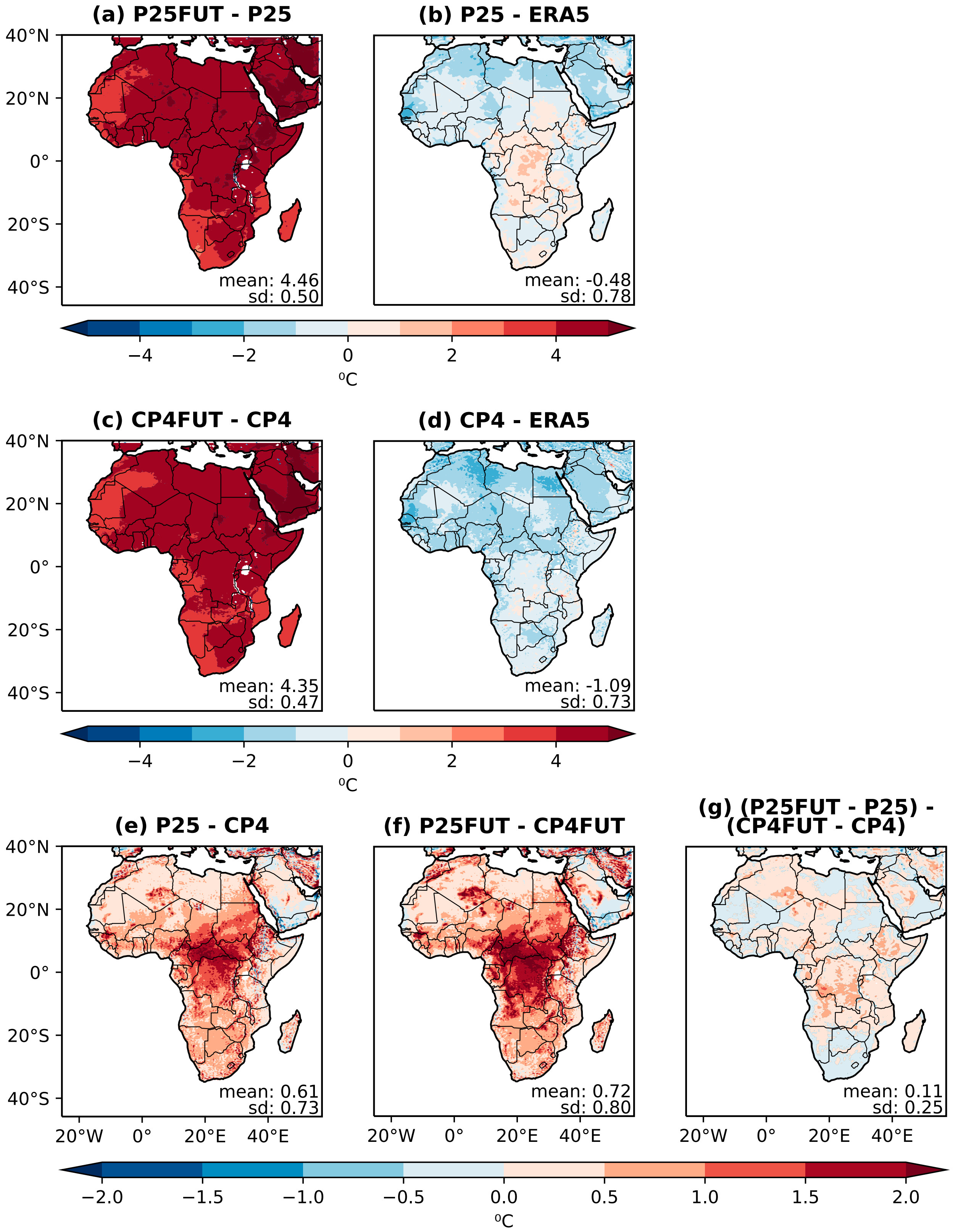

FIG. 6. Mean near-surface wet bulb temperature. (a),(d) mean future changes, (b),(d) difference between present-day model simulations and ERA5, and (e)–(g) differences between P25 and CP4 in the present day, future, and the future change.

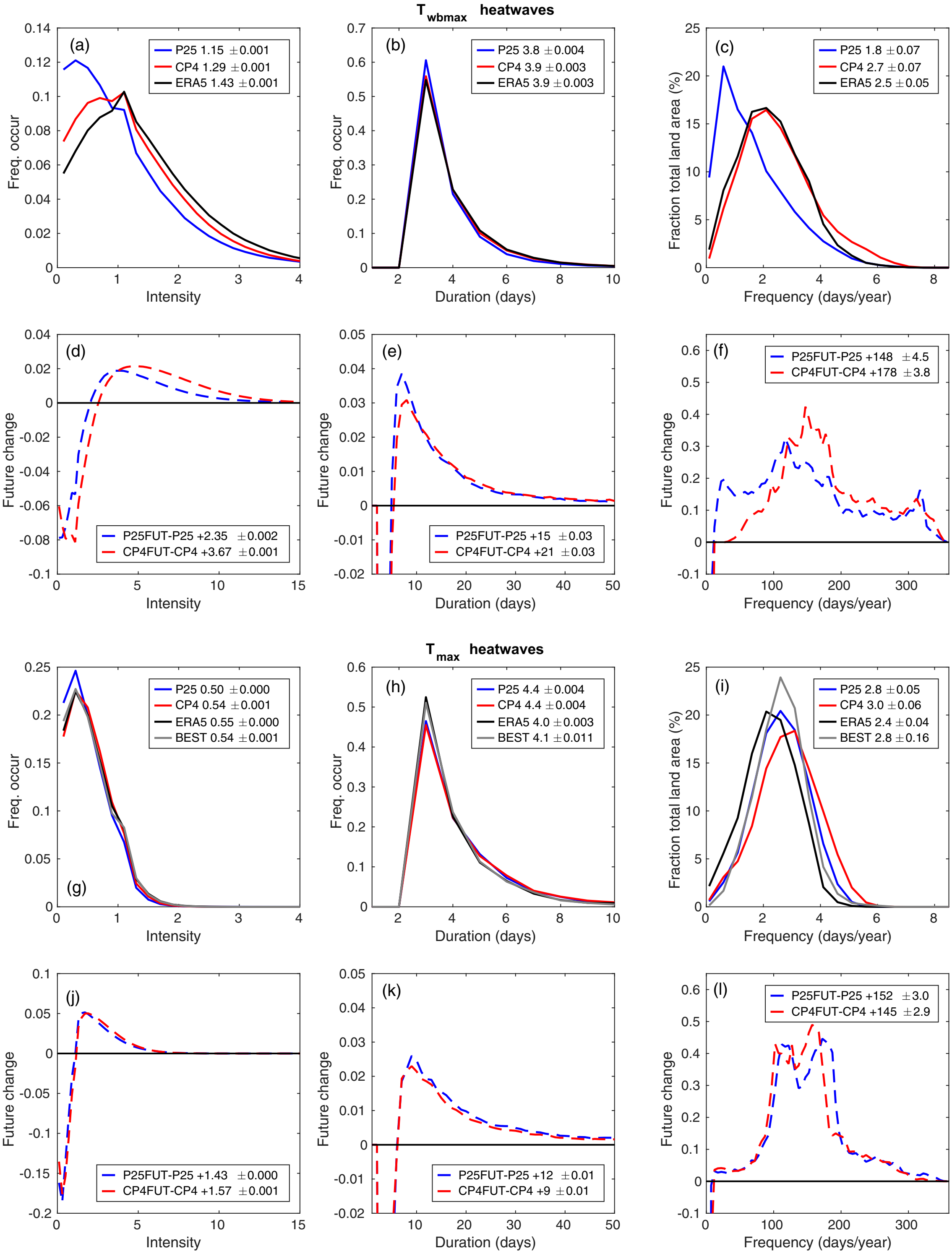

FIG. 7. Present-day and future change in pan-African heatwave metrics in ERA5, P25, CP4 (for both T_{wbmax} and $T_{\max}$ heatwaves), and BEST (for $T_{\max}$ heatwaves only): (a)–(c) present-day T_{wbmax} heatwaves, (d)–(f) future change in T_{wbmax} heatwaves, (g)–(i) present-day $T_{\max}$ heatwaves, and (j)–(l) future change in $T_{\max}$ heatwaves. All data are for the period 1997–2006. The numbers in the legends represent the mean and standard error of each distribution. The data in the intensity and duration distributions only include times and locations where heatwaves were diagnosed and are presented as a frequency of occurrence (i.e., the distribution is divided by the total number of heatwaves diagnosed). The frequency distribution is a count of the number of model grid boxes in each frequency bin.

therefore, in much better agreement with ERA5 (Fig. 7a). There is good agreement between P25, CP4, and ERA5 (and BEST for $T_{\max}$ heatwaves) for both T_{wbmax} and $T_{\max}$ heatwave duration, with present-day mean heatwave lengths of ~4 days (Figs. 7b and 7h). For frequency, there is reasonable agreement between the climate models and observations for $T_{\max}$ heatwaves, with on average 2.4–3.0 days yr^{-1} (Fig. 7i). For wet-bulb heatwaves, the distribution of heatwave frequency in P25 is skewed toward lower values, with a mean in P25 of 1.8 days yr^{-1} compared with values of 2.7 and 2.5 days yr^{-1} in CP4 and ERA5, respectively (Fig. 7c).

By 2100, under RCP8.5 both CP4 and P25 simulate large increases in all three metrics for both T_{wbmax} and $T_{\max}$ heatwaves. Considering both types of heatwaves and both model simulations, the ranges of future increases are from +1.5 to +3.7 for intensity, from +9 to +21 days for length, and from +145 to +178 days yr^{-1} for frequency (Figs. 7d–f,j–l). The frequency increase can be interpreted as, on average over all of Africa, up to half of all days of the year will experience heat and/or humidity conditions that currently only occur on the annual hottest/most humid 2–3 days. With such large increases, the future heatwave duration metric becomes inappropriate, and the focus should be on the total number of heatwave days per year (i.e., the frequency) and the intensity.

For T_{wbmax} heatwaves, the future change in intensity is 56% higher in CP4 than in P25 (Fig. 7d) and the future change in frequency is 20% higher in CP4 than P25 (Fig. 7f). For $T_{\max}$ heatwaves the future change in intensity is only 10% higher in CP4 than P25 (Fig. 7j) and the future change in frequency is actually 5% higher in P25 than CP4 (Fig. 7l). The model differences and future changes are broadly similar in all six of the subregions illustrated in Fig. 2 (not shown). Clearly there is much more disagreement between CP4 and P25 in the future change of T_{wbmax} heatwaves than $T_{\max}$ heatwaves. Processes such as moisture transport, cloud, evaporation, and rainfall are potentially key drivers of humid heatwaves, and it is known from previous work that moist processes are generally better represented in convective-scale models than models with parameterized convection (Finney et al. 2020; Finney et al. 2019; Jackson et al. 2020; Kendon et al. 2019). The following section diagnoses and compares the drivers of T_{wbmax} and $T_{\max}$ heatwaves over the African continent.

c. *Drivers of present-day wet- and dry-bulb heatwaves*

Figure 8 shows the mean annual cycle of ERA5 near-surface humidity, dry- and wet-bulb temperature, and GPM rainfall for the six subregions illustrated in Fig. 2. The $T_{\max}$ heatwaves occur most frequently in the months with the highest mean dry-bulb temperature, generally before the onset of the rainy season. For example, $T_{\max}$ heatwaves occur most frequently in the Gulf of Guinea (GoG) in February–April before the onset of the monsoon season in May/June. In contrast, T_{wbmax} heatwaves occur most frequently at least a month later, when temperatures are still hot but the humidity is beginning to increase. The difference in the timing of T_{wbmax} and $T_{\max}$ heatwaves is largest in the Sahel, where $T_{\max}$ heatwaves occur in March–May, consistent with previous studies (Barbier et al. 2018; Guigma et al. 2020; Largeron et al. 2020), but T_{wbmax} heatwaves occur most frequently in July–September, when the mean dry-bulb temperature is lower but the mean wet-bulb temperature and rainfall is highest.

It is important to understand if rainfall is a driver of and/or a response to humid heatwaves because it is known that models with parameterized convection struggle to represent rainfall frequency and intensity (Fiedler et al. 2020) and because there may be a growing risk of compound heat–flood hazards under climate change (Liao et al. 2021; You and Wang 2021). Figure 9 shows composites of the anomaly of wet day occurrence 5 days before (day −5) to 5 days after (day 5) the onset of T_{wbmax} and $T_{\max}$ heatwaves, relative to the weighted climatology of wet day occurrence (see section 2e). Wet days are defined as daily rainfall accumulations of >1 mm. Table 1 shows the percentage of T_{wbmax} and $T_{\max}$ heatwaves where the first day of the heatwave (day 0) is defined as a wet day, compared to the occurrence of wet days in the weighted climatology.

ERA5-GPM and all four climate model simulations show a positive anomaly in wet days between day −5 and day 5 after the commencement of T_{wbmax} heatwaves (Fig. 9a). For all heatwave–climatology rainfall pairs in Table 1 and Fig. 9, the Wilcoxon matched-pairs signed rank test shows that the rainfall distributions do not come from the same population ($p \ll 0.01$; see section 2f), so the differences in rainfall on heatwave days and in the climatology are statistically significant. The dots on Fig. 9 show where the anomalies are of the highest statistical significance (see Fig. 9 caption). The wet day anomaly in ERA5-GPM peaks between day 0 and day 3 of the heatwaves, whereas the peak in the climate models occurs the day before the onset of the heatwave (day −1).

It is not clear why there is a difference in the timing of the peak between ERA5-GPM and the models, which means that, in a pan-African sense at least, it is not clear whether rainfall drives T_{wbmax} heatwaves through evaporation or if the rainfall is a consequence of the increased humidity. However, evaporation from rain that falls during a T_{wbmax} heatwave is likely to help prolong it by maintaining higher levels of near-surface humidity. Splitting the plot into the six subregions provides more insight [see section 3d(2)].

In ERA5-GPM, T_{wbmax} heatwaves commence on wet days 32.3% of the time compared to an occurrence of wet days 22.9% of the time in climatology; that is, wet days occur almost 10% more often on the first day of a T_{wbmax} heatwave than they occur climatologically (Table 1). The pattern in the present-day climate models is similar but more extreme, with T_{wbmax} heatwaves commencing on wet days 56.5% of the time in P25 (compared to wet days occurring 34.8% of the time in climatology) and on wet days 35.0% of the time in CP4 (compared to wet days occurring 16.1% of the time in climatology). For both models, T_{wbmax} heatwaves commence about 20% more frequently on wet days than wet days occur in the climatology. The differences in the absolute percentages are due to the known differences in the distribution of rainfall intensity in the convective-scale and parameterized CP4 and P25 models, where parameterized models are known to have more frequent but lower rainfall rates compared to observations (see Table S1 for more details; Kendon et al. 2021; Kendon et al. 2014; Prein et al. 2015). Under climate change, the timing

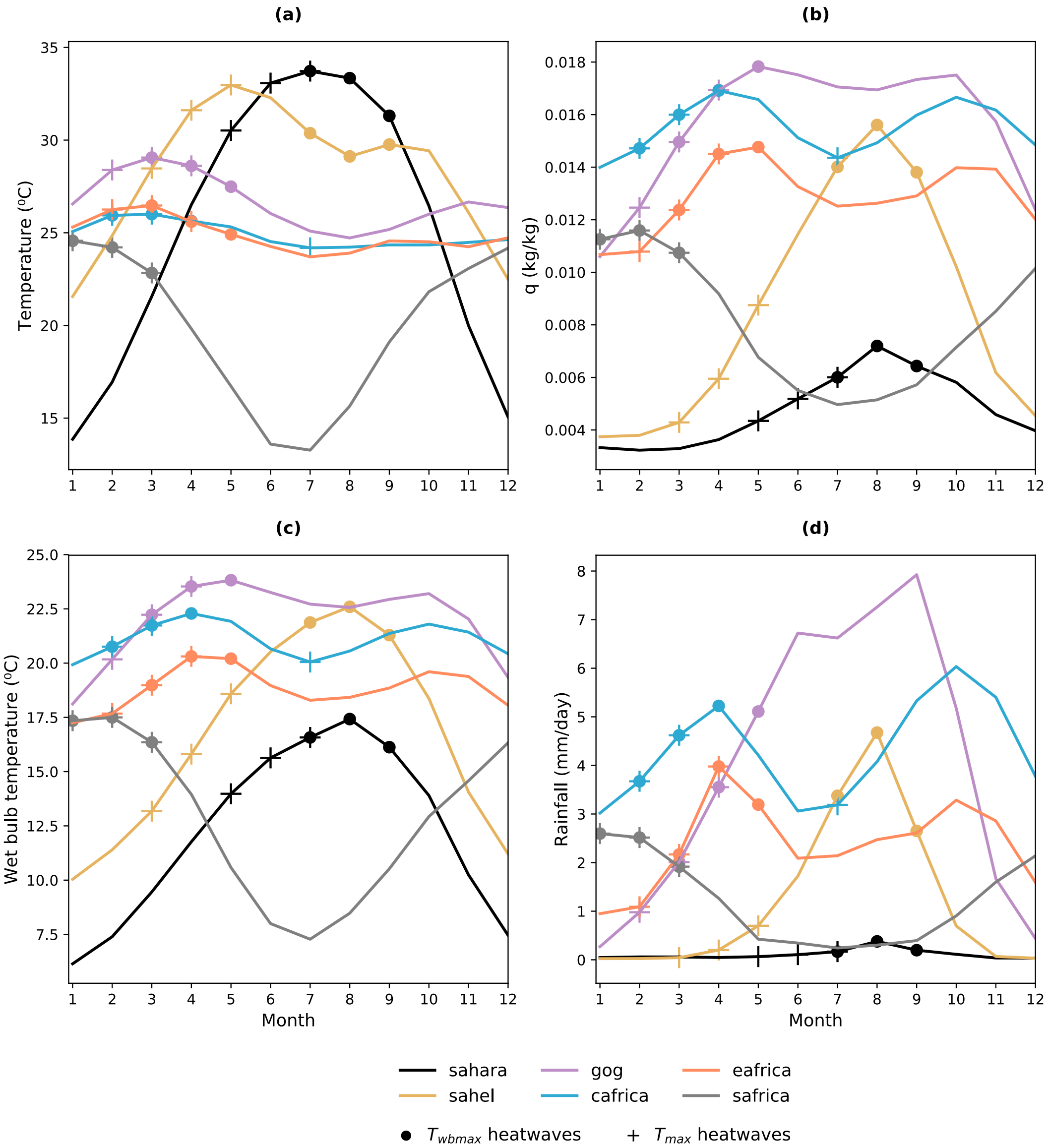

FIG. 8. Mean present-day annual cycles over the African subregions, as defined in Fig. 2a: (a) dry-bulb temperature, (b) wet-bulb temperature, (c), specific humidity from ERA5, and (d) rainfall from GPM. The dots and crosses represent the three months of the year in each region with the highest occurrence of present-day T_{wbmax} and T_{max} heatwaves, respectively.

of the peak in wet anomaly stays the same (Fig. 9a) but a larger percentage of T_{wbmax} heatwaves commence on wet days (change from 35.0% to 40.3% in CP4 and from 56.5% to 58.9% in P25), even though wet days occur approximately the same amount or even slightly less frequently in the climatology of the future simulations (Table 1).

The same relationship between present-day heatwaves and rainfall is not, however, apparent for T_{max} heatwaves. More than 5 days prior to heatwave onset there is a negative anomaly in wet day occurrence compared to climatology, which peaks at the onset of the heatwave (Fig. 9b). By day 5 (i.e., after most heatwaves have finished), the wet day occurrence has returned to the climatological value. In ERA5, 2.5% of T_{max} heatwaves commence on wet days, compared to wet days occurring on 11.1% of days climatologically (Table 1). Both CP4 and P25 are in broad agreement with ERA5, in that 0.8% and 3.0% of T_{max} heatwaves, respectively, commence on wet days, compared to wet days occurring 8.8% and 21.2% of the time, respectively, in the climatology. There is only a very small change in these percentages with climate change.

We now compare the drivers of T_{wbmax} and T_{max} heatwaves in ERA5. Figure 10 shows the mean anomalies of several key variables averaged over the first 3 days of each T_{wbmax} and T_{max} heatwave diagnosed in ERA5, relative to a weighted climatology (see section 2e). For T_{wbmax} heatwaves, the anomaly in daily mean dry-bulb temperature is relatively small (+0.32°C)

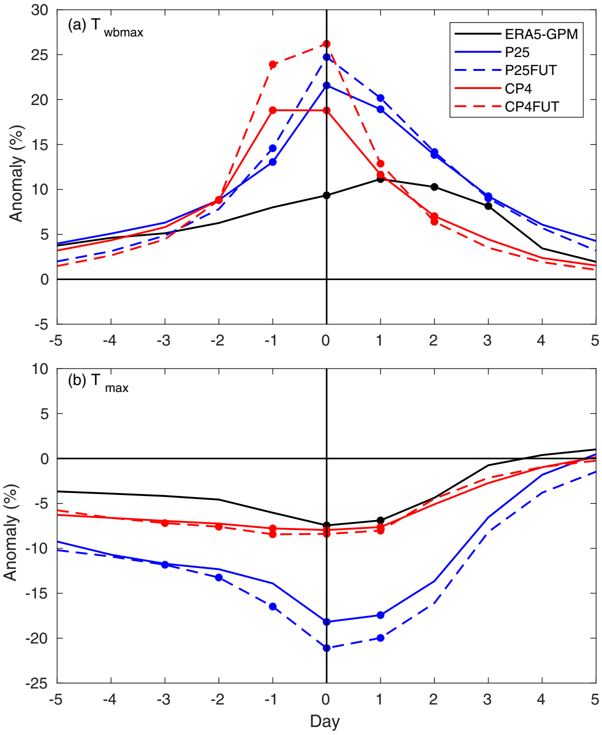

FIG. 9. Composite of wet day (>1 mm day^{-1}) occurrence during heatwaves minus wet day occurrence in the weighted climatology for (a) T_{wbmax} and (b) $T_{\max}$ heatwaves over the pan-African region. Day 0 is the first day of each heatwave. The climatological values take into account the fact that heatwaves do not occur uniformly in time or space. The climatology is computed by finding a mean of the frequency of occurrence of wet days in each rainfall category 15 days before and after each heatwave (day −15 and day 15). For ERA5 and the four climate model simulations, when considering the full datasets, the heatwave rainfall distributions from days −5 to 5 are all statistically significantly different to climatology (Wilcoxon matched-pairs signed rank test, $p \ll 0.01$; see section 2f), which shows that the rainfall distributions do not come from the same population. The days marked with a dot are when >90% of the Wilcoxon tests performed 10 000 times on 1000 randomly selected difference pairs have a p value of $p < 0.001$.

TABLE 1. Percentage of T_{wbmax} and $T_{\max}$ heatwaves associated with wet days (defined as daily rainfall accumulations of >1 mm). Data are presented for the first day of each heatwave and a climatological value for comparison, which is weighted for the months and locations in which the heatwaves occur: it is a mean of the rainfall 15 days prior to and 15 days after the first day of each heatwave. For all heatwave–climatology rainfall pairs the Wilcoxon matched pairs signed rank test shows that the rainfall distributions do not come from the same population ($p \ll 0.01$; see section 2f). An expanded version of this table, showing, for each model, the distribution of rainfall daily accumulations on the first day of each heatwave and the difference between the rainfall climatologies 15 days prior to and after the first day of each heatwave is presented in Table S1.

	T_{wbmax} (%)		$T_{\max}$ (%)	
	First day of heatwave	Climatology	First day of heatwave	Climatology
ERA5-GPM	32.3	22.9	2.5	11.1
CP4	35.0	16.1	0.8	8.8
CP4FUT	40.3	14.1	0.9	9.3
P25	56.5	34.8	3.0	21.2
P25FUT	58.9	34.1	2.7	23.8

and there is a large (+3.2 g kg^{-1}) anomaly in daily mean specific humidity (blue bars, Figs. 10a,b). The anomaly in top of atmosphere outgoing longwave radiation (OLR) is −12 W m^{-2}, which indicates increased cloud occurs during T_{wbmax} heatwaves compared to climatology. Increased cloud and moisture lead to a decrease in the surface net shortwave radiation flux, $\mathrm{SW_{net}}$, of 5 W m^{-2} and an increase in the surface net longwave radiation flux, $\mathrm{LW_{net}}$, of 15 W m^{-2}. The sensible heat flux, H, decreases by 8 W m^{-2} but the latent heat flux, E, increases by 18 W m^{-2}. The sum of the anomalies of the radiative terms approximately balances the sum of anomalies in the turbulent fluxes, both with a net anomaly of +10 W m^{-2} (right-hand blue bars, Fig. 10d). Humidity advection is positive (moistening) but small, at +0.025 g kg^{-1} day^{-1} (Fig. 10e) compared to the anomaly in mean humidity of +3.2 g kg^{-1}. Temperature advection is negative (cooling) and also small, at −0.022°C day^{-1} (Fig. 10f), compared to the anomaly in mean temperature of 0.32°C of the opposite sign.

Conversely, $T_{\max}$ heatwaves occur during much larger daily mean dry-bulb temperature anomalies of +3.2°C and dry specific humidity anomalies of −1.4 g kg^{-1}, compared to climatology. The OLR anomaly is +13 W m^{-2}, indicating lower, warmer cloud or a lower cloud fraction compared to climatology. $\mathrm{SW_{net}}$ increases by 13 W m^{-2} and $\mathrm{LW_{net}}$ decreases by a similar amount; H increases by 3.5 W m^{-2} and E decreases by 8.6 W m^{-2}. Humidity advection is negative (drying) but small, at −0.063 g kg^{-1} day^{-1} (Fig. 10e), compared to the anomaly in mean humidity of −1.4 g kg^{-1} (Fig. 10b). Temperature advection is positive (warming) but small, at +0.01°C day^{-1} (Fig. 10f), compared to the positive anomaly in mean temperature of 3.2°C (Fig. 10a).

In summary, in a pan-African sense, the main drivers of T_{wbmax} heatwaves are increased atmospheric moisture, cloud, and rainfall and a low Bowen ratio (high surface latent heat flux), leading to higher humidity and increased absorption of longwave radiation within the atmospheric column (i.e., the water vapor and cloud greenhouse effect). In contrast, $T_{\max}$ heatwaves are driven by decreased cloud cover, increased surface $\mathrm{SW_{net}}$, and a high Bowen ratio (high surface sensible heat flux). These results are based on reanalysis, which is itself a model with parameterized convection. It is likely that reanalysis is a better representation of dry-bulb heatwaves because they occur at times without cloud and rainfall because moist processes are more challenging to represent in models, especially those with parameterized convection (Fiedler et al. 2020).

Given the key role of moist processes in T_{wbmax} heatwaves, their importance for human health (Armstrong et al. 2019), the fact that the model difference between P25 and CP4 in the future

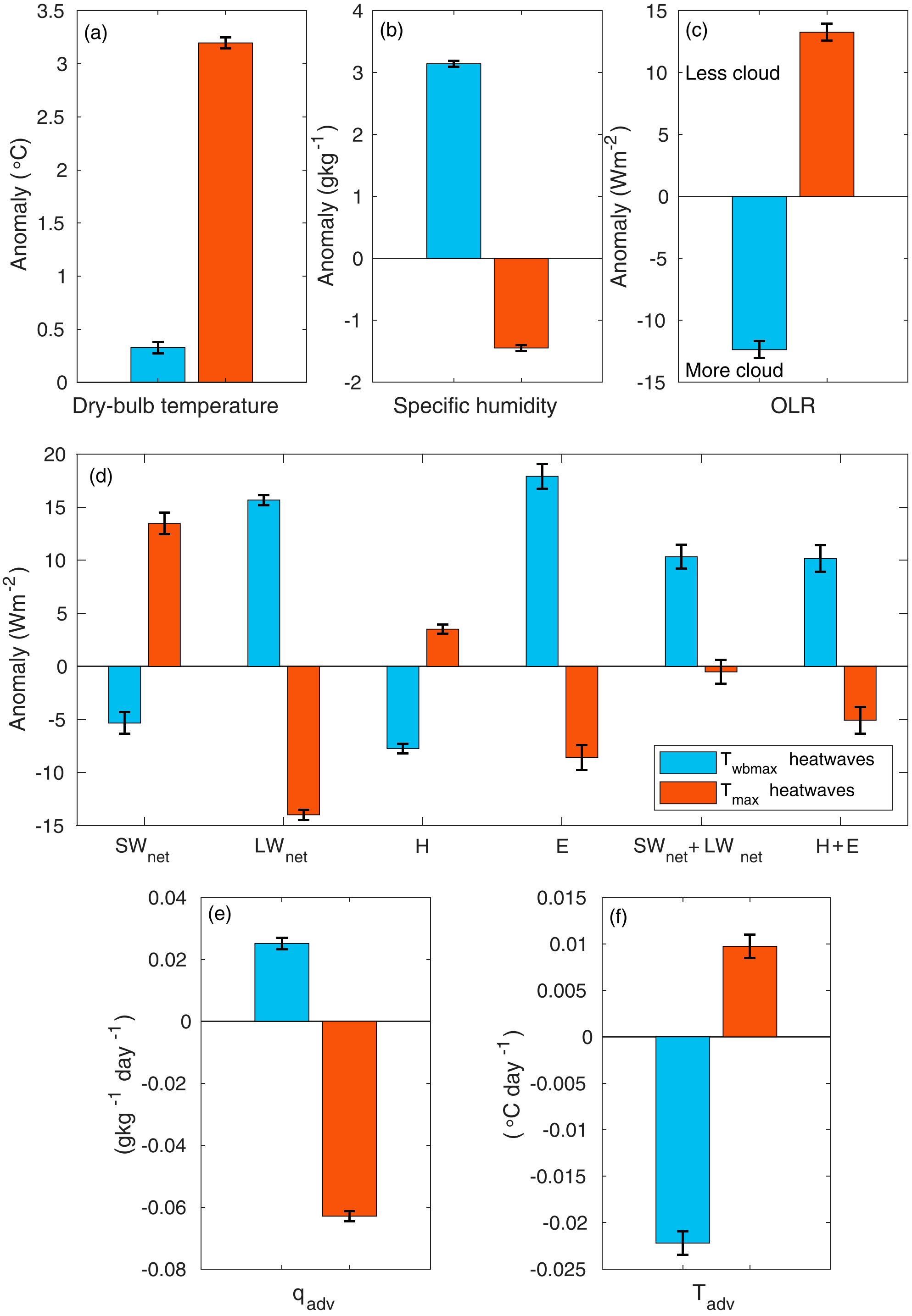

FIG. 10. Anomalies relative to climatology of key ERA5 variables over the pan-Africa region during T_{wbmax} and T_{max} heatwaves diagnosed in ERA5: (a) near-surface daily mean dry bulb temperature; (b) near-surface daily mean specific humidity; (c) outgoing longwave radiation; (d) surface net shortwave radiation, longwave radiation, sensible heat flux, latent heat flux, and the sum of the radiative and turbulent terms; (e) 850-hPa moisture advection; and (f) 850-hPa temperature advection. All variables are averaged over the first 3 days of each heatwave. All variables are presented as anomalies from the climatological annual cycle (see section 2e), apart from q_{adv} and T_{qdv}, which for ease of interpretation are the absolute values. The data for ERA5 are for heatwaves during the period 2001–19 to align with the availability of GPM rainfall data plotted in Fig. 9. The error bars represent the standard error.

change in T_{wbmax} heatwaves is much larger than for T_{max} heatwaves (Fig. 7), and the known differences in the representation of moist processes in convective-scale and convection-parameterized models, the remainder of the paper will focus on T_{wbmax} heatwaves. It will examine the heatwave metrics and drivers on a regional basis and the reasons why the convective-scale climate model projects a larger future change in T_{wbmax} heatwaves.

d. Regional analysis of T_{wbmax} heatwaves

1) SPATIAL VARIABILITY OF T_{WBMAX} HEATWAVES

Figure 11 shows maps of the present-day T_{wbmax} heatwave metrics in ERA5, P25, and CP4. The white speckling in the intensity and duration plots illustrates regions where no heatwaves are diagnosed in the entire 10-yr period. A diagnosis of no heatwaves is possible at locations where there are no occurrences of 3 consecutive hot days. No present-day heatwaves were diagnosed in 0.4% of ERA5 grid boxes, 4.4% of P25 grid boxes, and 1.0% of CP4 grid boxes. Intensity is fairly uniform to the south of the equator in all three datasets (Figs. 11a–c). ERA5 produces intensity hotspots in the Sahel and Sahara, whereas there are many grid boxes in P25 over the Sahel where no heatwaves are diagnosed over the 10-yr period. CP4 produces a spatial distribution of intensity closer to that in ERA5, with an intensity hotspot between 10° and 30°N, although it is not as intense as in ERA5. Hotspots of mean heatwave duration of five or more days and frequency of four or more heatwave days per year are apparent in ERA5 across the Sahel and Sahara, in East Africa, and along the southern African west coast (Figs. 11d,h). The spatial distribution in CP4 is again closer to the distribution in ERA5 than P25. The hot spot between 10° and 30°N in ERA5 is not apparent in P25; rather, it is a region of short duration or no heatwaves (Figs. 11e,f,i,j).

Maps of the future change in the three heatwave metrics in P25 and CP4, and the difference in the future change (P25 future change minus CP4 future change), are shown in Fig. 12. In both climate models there are hot spots in the future change of intensity along the equatorial belt between 20°S and 5°N, with particularly high values along the GoG coast (Figs. 12a,b). The highest values, of +3 or more, extend across most of sub-Saharan North Africa in CP4. Overall, the future change in intensity is larger almost everywhere in CP4 than P25 (mean changes of +3.67 in CP4 compared with +2.35 in P25; Fig. 7d), with the largest differences between the two model simulations 5°–15°N and 10°–20°S. There are some small patches near the equator where the change in P25 is greater than in CP4, consistent with the fact that P25 has a greater increase in total column water vapor nearer the equator, linked to model differences in the changing Hadley circulation (Jackson et al. 2020; see also Fig. 5g showing specific humidity).

There is a clear hotspot in the future change in frequency and duration over equatorial Africa (10°S–10°N) in both P25 and CP4, which tends to be larger in the more humid West African coast and central Africa/Congo rather than the drier East African region. The future change in duration outside this region is up to approximately +20 days; however, within the equatorial belt both models simulate values of greater than +80 days (Figs. 12d,e). The future change in duration in CP4 is larger overall compared to that in P25 (+21 and +15 days, respectively; Fig. 7e). The change is larger north of ~7°N in CP4, whereas the change is larger in P25 over GoG and parts of central Africa. The measure of duration does, however, break down under climate change as the number of heatwave days per year increases so much; therefore, it is better to focus on the intensity and frequency metrics.

There is good agreement between CP4 and P25 in the spatial distribution of the future change in frequency, with both models simulating future increases of more than +200 days yr^{-1} in the equatorial belt, with largest changes in humid regions, and values of more than +100 days yr^{-1} elsewhere (Figs. 12h,i). CP4 simulates larger future changes in frequency than P25 (means of +178 days yr^{-1} compared to +148 days yr^{-1}; Fig. 7f) everywhere apart from a small region in central Africa (Fig. 12j), again consistent with the greater total column water vapor increase seen in P25 in this region (Jackson et al. 2020).

In summary, the simulations show that by 2100 under RCP8.5, conditions experienced on the present-day wet-bulb heatwave days will be experienced consistently throughout the hottest/wettest three months of the year and over the equatorial belt, and these conditions will be experienced up to 50% of the time. The hot spot in the future change in T_{wbmax} heatwave frequency over equatorial Africa is consistent with previous global studies (Coffel et al. 2017; Mora et al. 2017) and is collocated with the area of largest future change in mean humidity, where humidity increases by more than 2 g kg^{-1} (compared to pan-African increases of $<+0.5$ g kg^{-1}; Figs. 5a,c).

2) T_{WBMAX} HEATWAVES AND RAINFALL

Figure 13 shows composites of wet day (>1 mm day^{-1}) occurrence relative to climatology around the time of the onset of T_{wbmax} heatwaves. There are larger, more statistically significant wet day anomalies over the relatively arid regions of the Sahara, Sahel, East Africa (EAfrica), and southern Africa (SAfrica). In the Sahara the peak in wet day anomaly coincides with the first day of the T_{wbmax} heatwave in all four datasets. ERA5-GPM wet days occur 23.6% of the time on the first day of a T_{wbmax} heatwave, compared to wet days occurring 4.3% of the time in the weighted climatology (the day 0 percentages for all models and regions are shown in Table S2). In the Sahel, EAfrica, and SAfrica the picture is less clear with wet day anomalies peaking between day −1 and day 1 depending on the dataset.

GoG and central Africa (CAfrica) have different behavior, with smaller positive wet day anomalies in the four climate model simulations and negative anomalies in ERA5-GPM between day −1 and day 1. GoG and CAfrica can be considered as moist equatorial regions, and experience a relatively low-amplitude annual cycle of humidity and wet-bulb temperature and a relatively high mean annual rainfall (Figs. 8b–d). Although EAfrica is also within the equatorial belt, it is generally more arid than GoG and CAfrica, with a

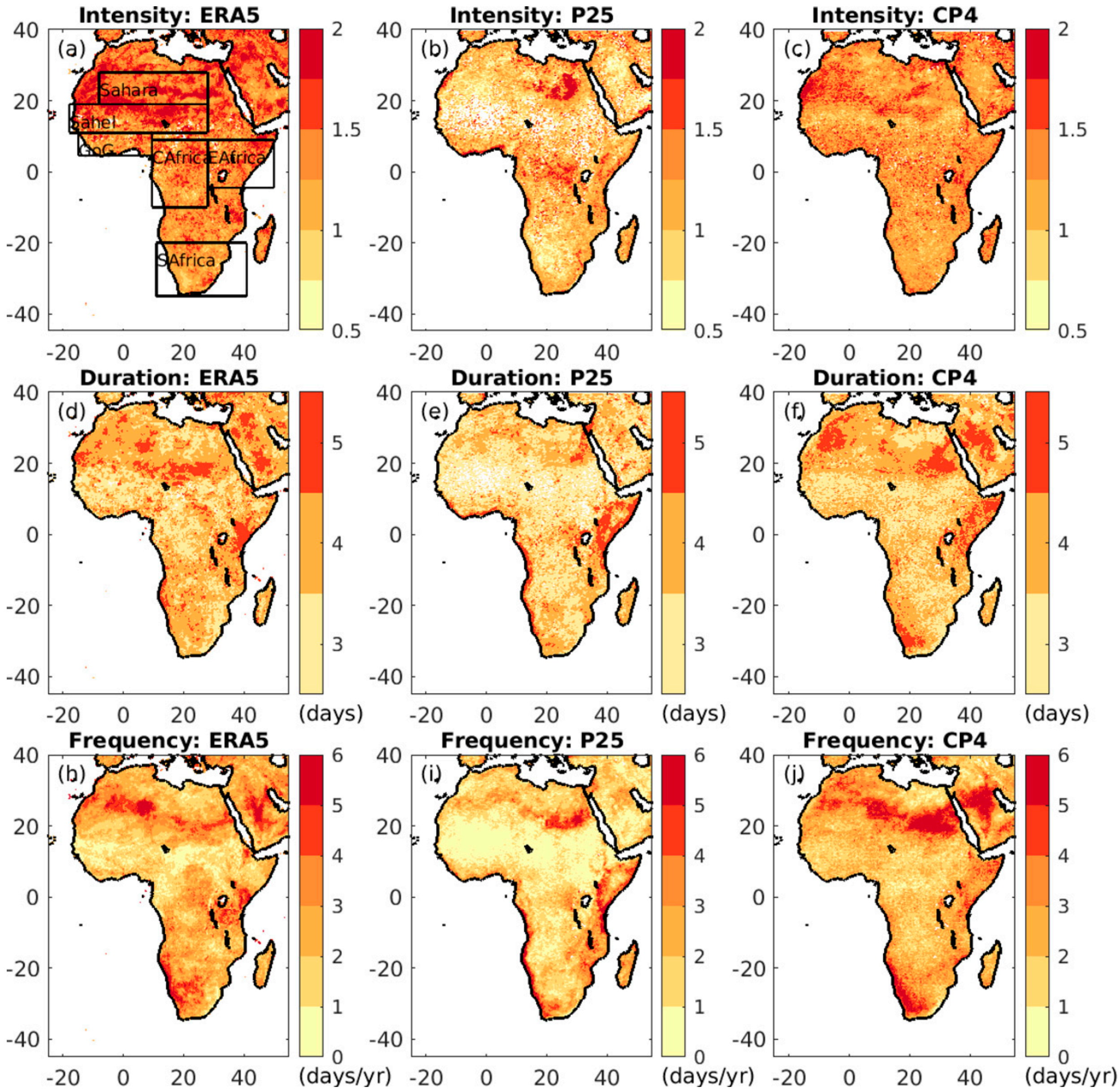

FIG. 11. Present-day T_{wbmax} heatwave metrics: (a)–(c) intensity, (d)–(f) duration, and (h)–(j) frequency for (left) ERA5, (center) P25, and (right) CP4. The boxes in (a) show the analyzed subregions. The white speckled pixels are regions where no heatwaves in 10 years were diagnosed.

lower-amplitude mean annual cycle of humidity but more moderate rainfall.

Apart from in the Sahara, the percentage of T_{wbmax} heatwaves associated with wet days decreases or stays almost the same under climate change in all regions and both climate models (Fig. 13 and Table S2). Climatologically, the number of wet days decreases in both P25 and CP4 (Table S2). The exceptions are in the Sahara, where wet days increase in both P25 and CP4 and in EAfrica, where they increase in P25. A broad decrease in wet days is consistent with Kendon et al. (2019), who report future increases in dry spell length in the same set of climate model simulations.

3) DRIVERS OF T_{WBMAX} HEATWAVES

Figure 14 shows the anomalies of key variables averaged over the first 3 days of each T_{wbmax} heatwave, separately for each subregion and for ERA5 only. Unlike the equivalent plot for T_{max} heatwaves (Fig. S2), there are large regional differences in the sign of the anomalies in the T_{wbmax} heatwave plot. The Sahel experiences negative dry-bulb temperature

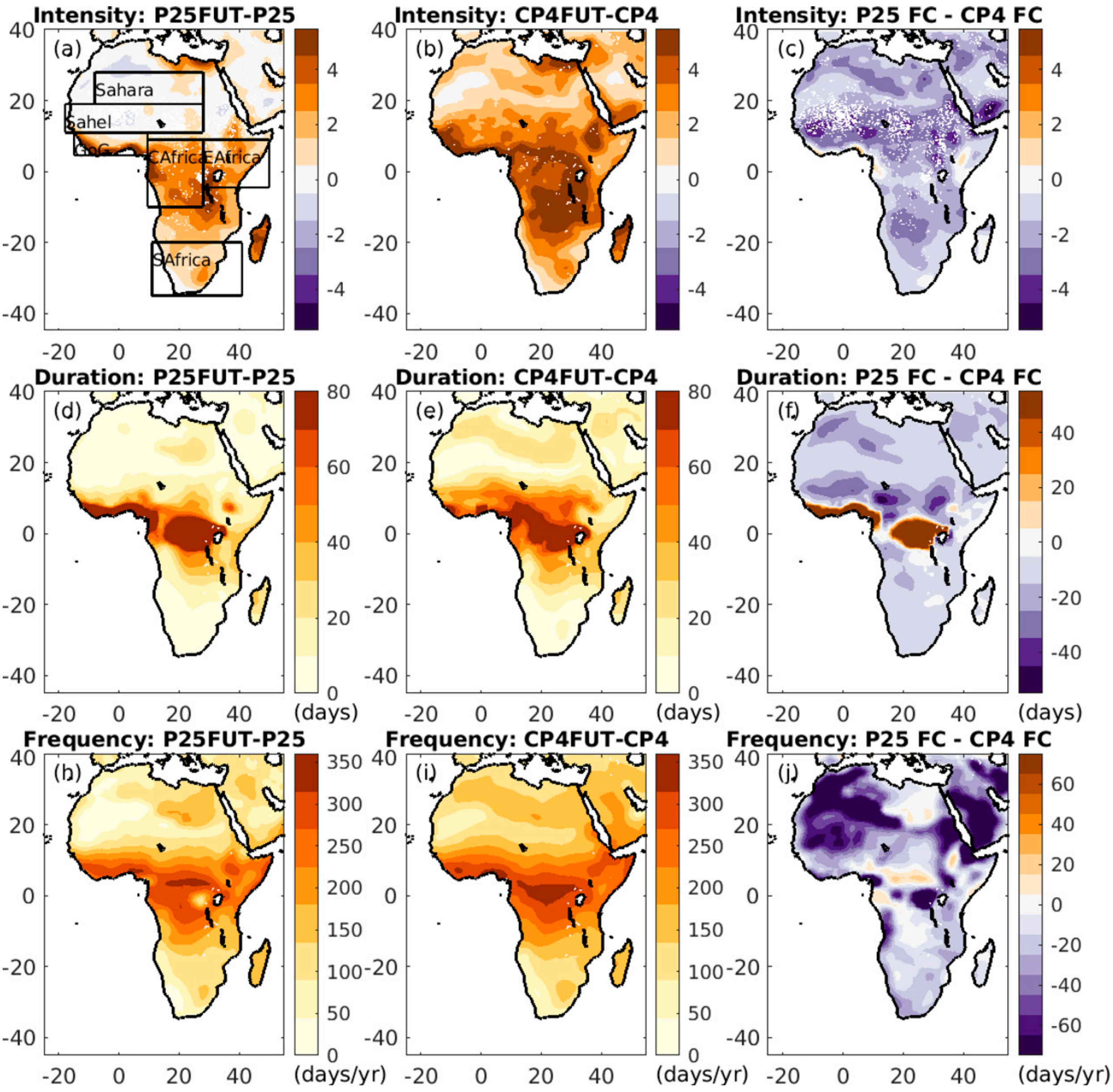

FIG. 12. Future change in T_{wbmax} heatwave metrics: (a)–(c) intensity, (d)–(f) duration, and (h)–(j) frequency for (left) P25, (center) CP4, and (right) the difference in the future change (left minus center). The boxes in (a) show the analyzed subregions.

anomalies (i.e., cooler than climatology), whereas the equatorial regions of GoG and CAfrica experience positive dry-bulb temperature anomalies during T_{wbmax} heatwaves (Fig. 14a). Dry-bulb temperature anomalies in the other regions are small. There are positive anomalies in specific humidity in all six regions; however, the magnitude is smaller over the already humid GoG and CAfrica.

Equatorial GoG and CAfrica also behave differently from the other regions in terms of the anomalies in OLR and the surface energy budget terms (Fig. 14c). GoG and CAfrica experience small positive anomalies in OLR (i.e., decreased cloud), which leads to positive anomalies in $\mathrm{SW_{net}}$, near-zero anomalies in $\mathrm{LW_{net}}$, near-zero anomalies in H, and a small positive anomaly in E. Conversely, the other regions experience large negative anomalies in OLR (i.e., increased cloud), which drives negative $\mathrm{SW_{net}}$ anomalies, positive $\mathrm{LW_{net}}$ anomalies, negative H anomalies, and large positive E anomalies. Moisture and temperature advection (shown as absolute values, rather than anomalies, for ease of interpretation in Figs. 14e and 14f) are small in all five regions.

In summary, the key T_{wbmax} heatwave drivers in the Sahara, Sahel, EAfrica, and SAfrica are broadly the same as the pan-African mean in Fig. 10, where high humidity, increased cloud, increased rainfall, latent heat flux, and longwave warming in the

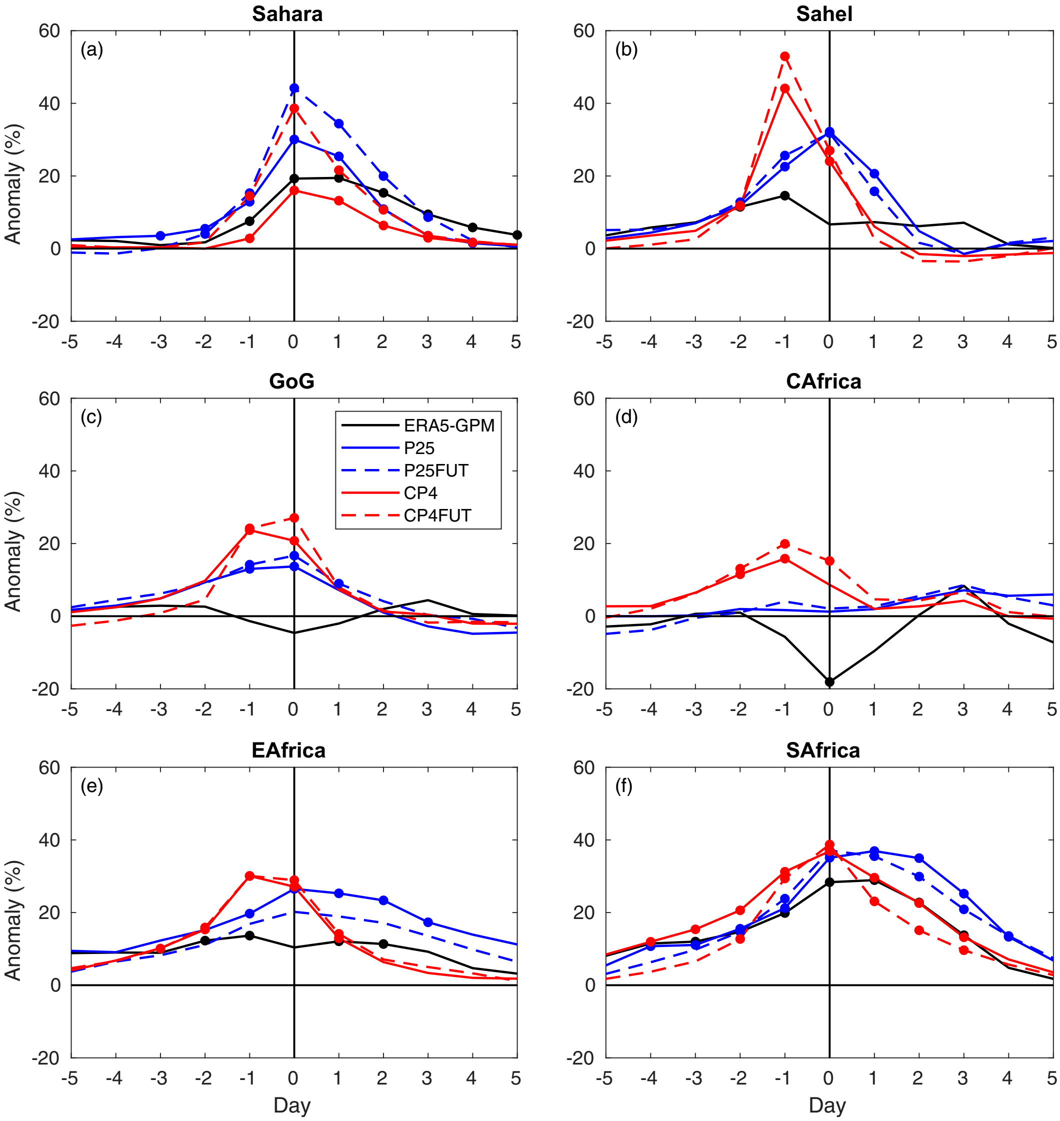

FIG. 13. Composites of wet day (>1 mm day^{-1}) occurrence during heatwaves minus wet day occurrence in the weighted climatology for $T_{\rm wbmax}$ heatwaves only of the six subregions. Day 0 is the first day of each heatwave. The dots represent the days with the largest differences between the heatwave and climatological rainfall distributions (see the caption of Fig. 9 for more details). The rainfall climatologies are computed in the same way as in Fig. 9.

atmospheric column are important. In the equatorial regions of GoG and CAfrica, where humidity is climatologically the highest, $T_{\rm wbmax}$ heatwaves are driven by a mixture of high temperature and humidity, with decreased cloud and increased shortwave warming.

4) FUTURE CHANGE IN HEATWAVE DRIVERS

Now we examine the future change in $T_{\rm wbmax}$ heatwave drivers in P25 and CP4 in order to understand why CP4 simulates a larger future change in $T_{\rm wbmax}$ heatwaves over almost all parts of Africa. We examine two regions: the Sahel, a region outside of the equatorial belt, where CP4 simulates a much larger future change in heatwave intensity and frequency than P25 (Fig. 15), and CAfrica, a region within the equatorial belt (i.e., within the future change "hotspot"), where the simulated future change in P25 and CP4 is more similar (Fig. 16). Plots of the other regions are shown in Figs. S3–S5, where GoG behaves broadly like CAfrica, and the Sahara, SAfrica, and EAfrica behave broadly like the Sahel. In Figs. 15 and 16, the future $T_{\rm wbmax}$ heatwaves are diagnosed using a future climate (rather than present day) baseline (see section 2c) and the anomalies are relative to present-day climatology.

In the Sahel, the dry-bulb temperature during $T_{\rm wbmax}$ heatwaves relative to present-day climatology increases by 6.3° and 5.0°C in P25 and CP4, respectively, under climate change (Fig. 15a). The specific humidity anomaly also increases in both models but to a larger extent in CP4 (9.3 g kg^{-1} in P25

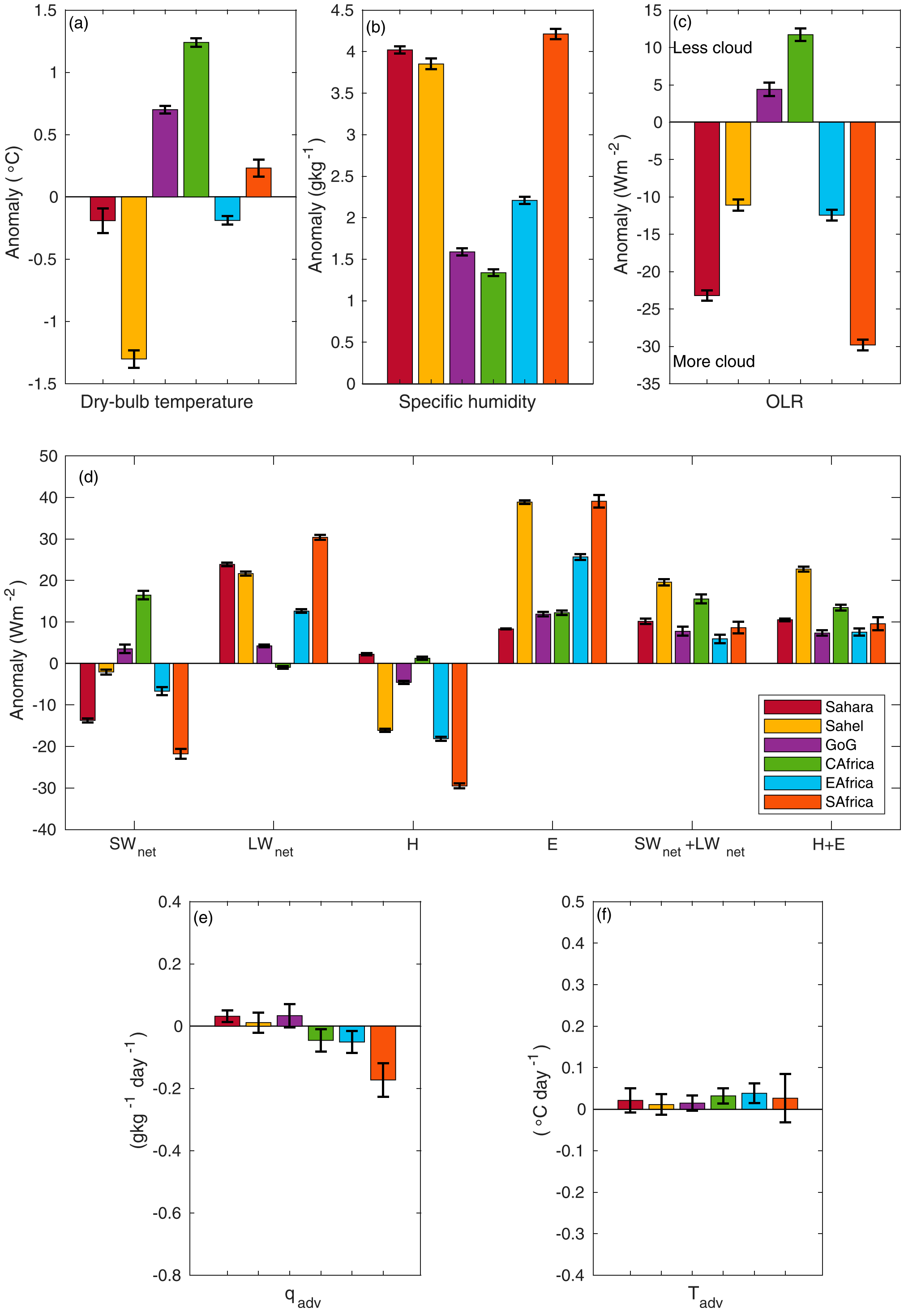

FIG. 14. Anomalies relative to climatology of key ERA5 variables by subregion during present-day ERA5 T_{wbmax} heatwaves: (a) near-surface daily mean dry-bulb temperature; (b) near-surface daily mean specific humidity; (c) outgoing longwave radiation; (d) surface net shortwave radiation, longwave radiation, sensible heat flux, latent heat flux, and the sum of the radiative and turbulent terms; (e) 850-hPa moisture advection; and (f) 850-hPa temperature advection. All variables are averaged over the first 3 days of each heatwave. All variables are presented as anomalies from the climatological annual cycle (see section 2e), apart from q_{adv} and T_{qdv}, which for ease of interpretation are the absolute values. The data for ERA5 are for heatwaves during the period 2001–19 to align with the availability of the GPM rainfall data plotted in Fig. 13. The error bars represent the standard error.

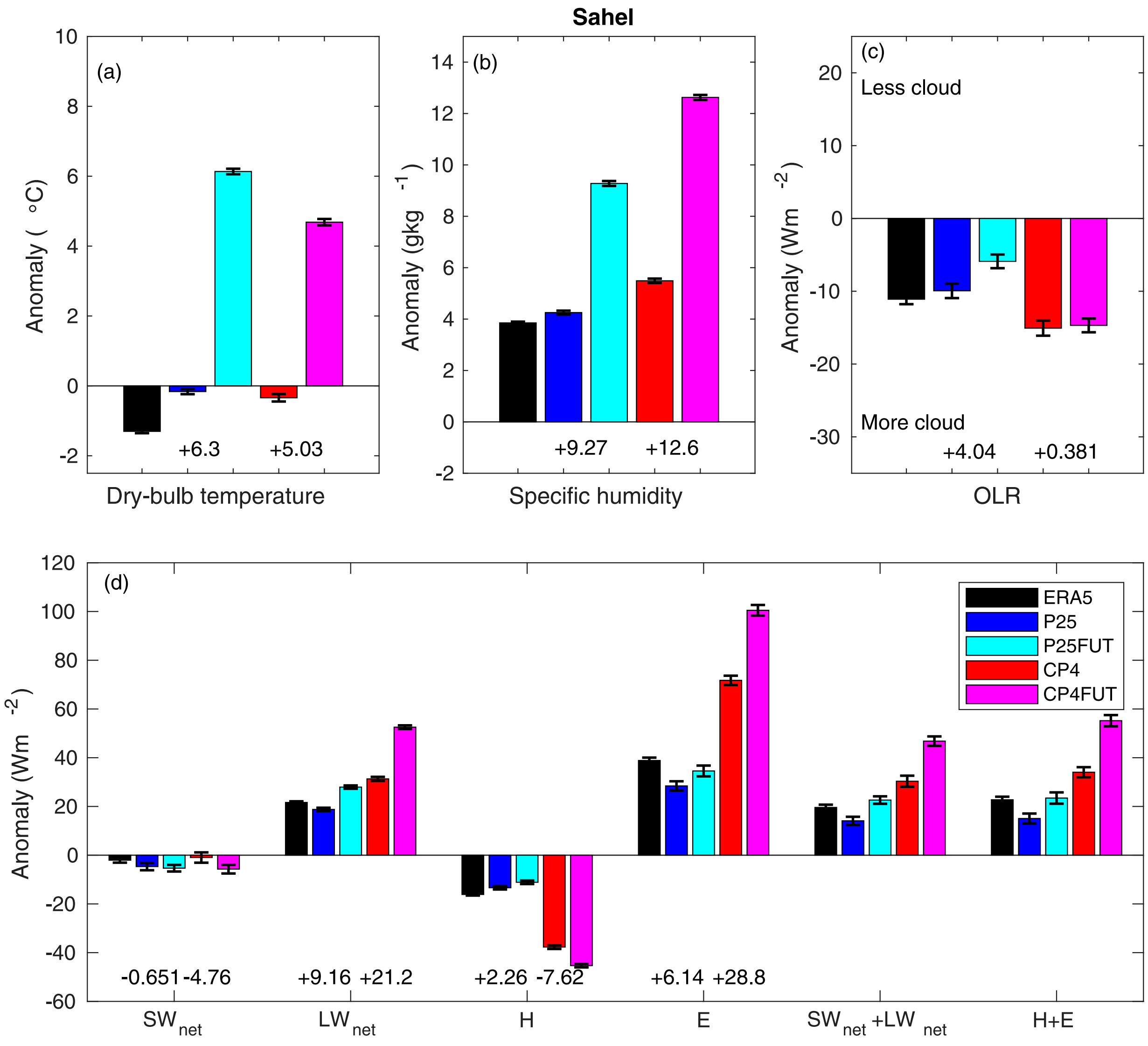

FIG. 15. Mean anomalies of key variables averaged over the first 3 days of each T_{wbmax} heatwave over the Sahel, relative to a representative mean annual cycle (see section 2e) for ERA5 and the four climate model simulations. The bars for P25FUT and CP4FUT represent heatwaves diagnosed using the future climate baseline (see section 2c) and are anomalies from the present-day annual cycle. The numbers under the P25 and CP4 present-day/future climate bar pairs show the future change in the anomaly of each variable. The error bars represent the standard error.

compared to 12.6 g kg^{-1} in CP4; Fig. 15b). Cloud during T_{wbmax} heatwaves decreases slightly in the future in both P25 and CP4; that is, the future heatwaves occur over slightly less cloudy skies (Fig. 15c). The main difference between P25 and CP4 is the increase in LW$_{\mathrm{net}}$ warming and the increase in latent heat flux (Fig. 15d). The future increase in LW$_{\mathrm{net}}$ warming is 9.2 W m^{-2} in P25 and 21.2 W m^{-2} in CP4 and the future increase in latent heat flux is 6.1 W m^{-2} in P25 and 28.8 W m^{-2} in CP4; both of these increases are much larger in CP4 than P25. For the present-day anomalies, P25 is generally in better agreement with ERA5 than CP4. However, given that ERA5 is also produced from a model with parameterized convection, in a region with limited in situ observations, it is not possible to determine whether P25 or CP4 is a better representation of reality.

In CAfrica, the future increases in the dry-bulb temperature and specific humidity anomalies are similar in P25 and CP4 and are on the order of +5°–6°C and +7–8 g kg^{-1}, respectively (Figs. 16a and 16b). Cloud cover becomes even less prevalent during T_{wbmax} heatwaves in the future (i.e., the heatwaves occur over clearer skies), and this change is larger in P25 (+10.9 W m^{-2}) than CP4 (+5.68 W m^{-2}). The P25 − CP4 difference in the future change in the anomalies in Fig. 16d is much smaller in CAfrica than the Sahel. For example, the future change in LW$_{\mathrm{net}}$ anomaly is +9.2 and +10.4 W m^{-2} for P25 and CP4, respectively, in CAfrica, compared to

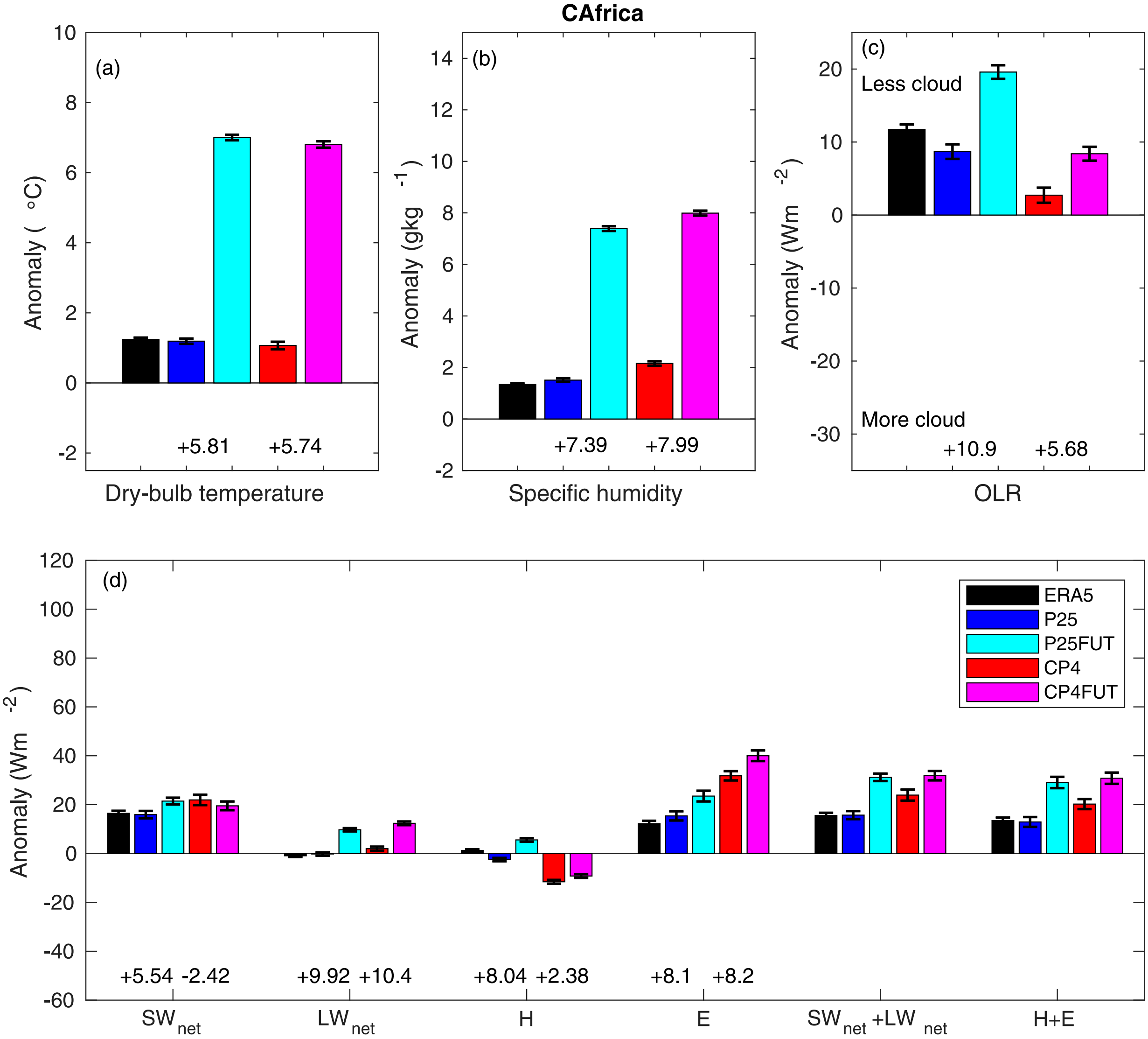

FIG. 16. As in Fig. 15, but for CAfrica.

+9.1 and +21.1 W m^{-2} in the Sahel. This is also the case for the latent heat flux, where the values in CAfrica are +8.1 and +8.2 W m^{-2} for P25 and CP4, respectively, compared to +6.1 and +28.8 W m^{-2} in the Sahel.

4. Discussion and conclusions

The present-day and future wet- and dry-bulb heatwaves are assessed in 10-yr convective-scale (CP4; 4.5 km) and parameterized convection (P25, 25km) simulations over the entire African continent. Compared to reanalysis, CP4 better reproduces the intensity and frequency of wet-bulb heatwaves (and their spatial distribution) than P25. For dry-bulb heatwaves, the difference between the two climate model simulations is much smaller, with both in good agreement with reanalysis and observations.

Both CP4 and P25 show large increases in the intensity, duration, and frequency of dry- ($T_{\max}$) and wet-bulb (T_{wbmax}) heatwaves by 2100 under RCP8.5. Present-day conditions that occur on 3–6 heatwave days per year are expected to be normal by 2100, occurring on 150–180 days per year. Huge future increases such as this are consistent with previous global and regional studies (Coffel et al. 2017; Mora et al. 2017; Russo et al. 2017).

P25 and CP4 simulate similar future changes in $T_{\max}$ heatwaves; however, the future change in T_{wbmax} heatwaves is larger in CP4 than P25: future changes in intensity are +3.67 compared to +2.35 and future changes in frequency are +178 days yr^{-1} compared to +148 days yr^{-1}. The difference in the future change between the two model simulations occurs despite very similar future increases in the mean specific humidity and dry-bulb temperature. Both CP4 and P25 have a cold and dry bias in their mean climate, which is common for climate models in the tropics (Zhao et al. 2015). These biases in the mean climate will cause absolute values of wet-bulb temperature to be biased too low, which is not an issue for the percentile-based heatwave metric used in this study but is an issue for measures of humid heatwaves that use absolute thresholds, such as the survivability threshold of 35°C in wet-bulb temperature, where sweating becomes ineffective (Sherwood and Huber 2010). Bias correction may not be possible due to the lack of routine humidity observations over Africa.

This study uses reanalysis to document the differences in the present-day drivers of T_{max} and T_{wbmax} heatwaves over the entire African continent. The timing of T_{max} and T_{wbmax} heatwave events within the annual cycle is different. The T_{max} heatwaves occur in the warm and dry premonsoon months, such as March–May in the Sahel, consistent with previous literature (Barbier et al. 2018; Fontaine et al. 2013; Guigma et al. 2020), whereas T_{wbmax} heatwaves tend to occur at the start and/or during the rainy season (July–September in the Sahel), when temperatures remain reasonably high but humidity increases.

African T_{max} heatwaves are associated with low rainfall (only 2.5% of T_{max} heatwaves commence on wet days), decreased humidity and cloud, higher shortwave surface warming, and a high sensible heat flux. This is in broad agreement with Bouniol et al. (2021) and Hong et al. (2018), who both found similar drivers from observations for T_{max} heatwaves over the Sahel and the Korean Peninsula, respectively. In contrast, African T_{wbmax} heatwaves are associated with much larger humidity anomalies than dry-bulb temperature anomalies. They are associated with rainfall, increased cloud and humidity, increased evaporation, and increased longwave warming within the atmospheric column (i.e., the greenhouse warming effect). In ERA5, 32% of T_{wbmax} heatwaves commence on wet days, compared to wet days occurring 23% of the time in a weighted climatology. Through the process of evaporation, soil moisture could be a key driver of African humid heatwaves during the wet season and should be a focus of future research. In a pan-African sense, moisture and temperature advection appear to play only a limited role in both types of heatwaves.

The T_{wbmax} heatwave drivers documented here, which are associated with moist processes, are similar to those diagnosed by Bouniol et al. (2021) for daily minimum dry-bulb temperature (T_{min}) heatwaves. Given that both T_{min} and T_{wbmax} heatwaves are associated with increases in humidity, it is possible that the differences between P25 and CP4 for T_{min} heatwaves would be the similar to those documented here for T_{wbmax} heatwaves. Bouniol et al. (2021) also found reduced and increased aerosol load during T_{max} and T_{min} heatwaves, respectively. Dust and aerosol are not considered in this study, but their impact on T_{wbmax} heatwaves should be explored in future work.

Both P25 and CP4 simulate a hot spot of large future change in T_{wbmax} heatwaves over the equatorial regions of Africa, consistent with previous research on humid heatwaves (Coffel et al. 2017; Mora et al. 2017). This hotspot is collocated with a large future increase in mean specific humidity over the equator in both models. This study, for the first time, compares the drivers of present day T_{wbmax} heatwaves over different regions of Africa. Outside the equatorial belt, the drivers of T_{wbmax} heatwaves are similar to the pan-African mean described above. The equatorial belt is climatologically moister and experiences higher rainfall than elsewhere. In contrast to elsewhere, T_{wbmax} heatwaves here are driven by both temperature and humidity anomalies (rather than predominantly by humidity). The heatwaves occur under increased shortwave surface heating at the same time as increased evaporation from rainfall. Large regional variations in the drivers of African humid heatwaves (relative to the more consistent drivers of T_{max} heatwaves) is consistent with the findings of Raymond et al. (2021), who studied a number of different regions around the world.

The results from this study highlight the potential for an increase in co-occurring or consecutive events ("compound hazards") of African heatwaves, heavy rainfall, and flooding, as has been observed in other regions such as China and the United States (Liao et al. 2021; Raghavendra et al. 2019; You and Wang 2021). Both P25 and CP4 simulate future increases in the percentage of T_{wbmax} heatwaves that occur on days with >10 mm daily rainfall accumulations. In CP4 this increase extends to days with >50 mm daily rainfall accumulations (Table S1). Humid heat events occurring at the same time as heavy rainfall and flooding could potentially overwhelm road, hospital, and power infrastructure and lead to a higher number of fatalities and more economic damage than if these events occurred in isolation (Zhang and Villarini 2020).

The T_{wbmax} heatwaves are driven by moist processes. The fundamental difference between CP4 and P25 model configurations is the representation of convection, so the reason for the larger future change in humid heatwaves in CP4 must originate from its representation of moist processes. CP4 simulates larger anomalies than P25 in almost all the key T_{wbmax} heatwave drivers (temperature, humidity, cloud, rainfall, radiation, turbulent fluxes) in the future compared to the present day. This is true in all the sub regions apart from the equatorial regions of central Africa and the Gulf of Guinea, where the difference in the future change in T_{wbmax} heatwaves in P25 and CP4 is much smaller. Previous studies show that convective-scale climate models are better able to represent extremes and respond realistically to environmental controls, giving a greater intensification of rainfall under climate change (Ban et al. 2020; Birch et al. 2014a; Chan et al. 2016; Finney et al. 2020; Finney et al. 2019; Fitzpatrick et al. 2020b; Jackson et al. 2020; Prein et al. 2015).

Climate models with parameterized convection, such as those used in the Coupled Model Intercomparison Project (CMIP), have similar issues with moist processes as P25 (Fiedler et al. 2020), so CMIP projections may also underestimate the future change in humid heatwaves. This heightens the need for mitigation and adaptation strategies and also indicates that, if anything, there is even less time available to implement such changes to avoid catastrophic future heat conditions than previously thought.

The analysis in this study has highlighted that it is critical to account for the fact that the mean diurnal cycle of humidity is out of phase with the mean diurnal cycle of dry-bulb temperature: specific humidity peaks overnight but dry-bulb temperature peaks during the day. Previous studies using CMIP5 models (Coffel et al. 2017; Russo et al. 2017), for example, necessarily use daily mean specific humidity to convert daily maximum dry-bulb temperature to daily maximum wet-bulb temperature, because subdaily diagnostics are generally unavailable. Analysis in this study shows that the values of daily maximum wet-bulb temperature and the subsequent heatwave diagnostics that are computed can be very sensitive to the way the daily maximum wet-bulb temperature is computed. Climate model simulations that are run in the future should, if practical, output hourly temperature and humidity data, or implement the computation of heat stress metrics within the model simulation, as recommended by Buzan et al. (2015).

Acknowledgments. This work was funded by the Department for International Development/Natural Environment Research Council via the Future Climate for Africa (FCFA) funded project Improving Model Processes for African Climate (IMPALA, NE/M017214/1 and NE/MO17176/1) and U.K. Research and Innovation as part of the Global Challenges Research Fund (GCRF African SWIFT, NE/P021077/1). Marsham and Finney were also funded via the FCFA HyCRISTAL (NE/M019985/1) project and Marsham by AMMA-2050 (NE/M019977/1). Kendon gratefully acknowledges funding from the Joint U.K. BEIS/Defra Met Office Hadley Centre Climate Programme (GA01101). Keane was supported by the Centre for Environmental Computation and Modelling (CEMAC), University of Leeds. Birch and Chapman were also supported through the Global Challenges Research Fund, AFRICAP programme, Grant BB/P027784/1. We are grateful for the use of the Centre for Environmental Data Analysis (CEDA)-Jasmin computing facilities, ERA5 data from the Copernicus Climate Change Service (C3S) Climate Data Store, GPM-IMERG data from Goddard Earth Sciences Data and Information Services Centre, temperature observations from Berkeley Earth and the Climatic Research Unit, and weather station observations from Niger through AMMA-CATCH, from South Africa through FLUXNET and from the station in central Sudan.

Data availability statement. A subset of the CP4 and P25 climate model data used in this study is freely available from the Centre for Environmental Data Analysis at https://catalogue.ceda.ac.uk/uuid/a6114f2319b34a58964dfa5305652fc6, IMPALA: Improving model processes for African climate, as cited in Senior (2019a,b,c,d). The full dataset is also freely available, but due to its size, contact the lead author of this paper for access. Daily maximum temperature observations used in this study are openly available from the Berkeley Earth Surface Temperature gridded dataset at http://berkeleyearth.org/data/ as cited in Rohde and Hausfather (2020). The monthly mean temperature observations used in this study are openly available from the Climatic Research Unit at https://crudata.uea.ac.uk/cru/data/hrg/ as cited in Harris et al. (2020). The weather station data from Demokeya, Kordofan, central Sudan are freely available from https://doi.org/10.7167/2013/297973 as cited in Ardö (2013), the data from Banizoumbou, Niamey, Niger are freely available from AMMA-CATCH at http://bd.amma-catch.org/ as cited in Lebel et al. (2009), and the data from Skukuza, South Africa, are available from https://fluxnet.org/. The daily satellite rainfall retrievals used in this study are freely available from Goddard Earth Sciences Data and Information Services Centre at https://disc.gsfc.nasa.gov/datasets/GPM_3IMERGDF_06/summary, as cited in Huffman et al. (2014). The ERA5 reanalysis data are also freely available from the Copernicus Climate Change Service (C3S) Climate Data Store at https://doi.org/10.24381/cds.adbb2d47 and https://doi.org/10.24381/cds.bd0915c6 as cited in Hersbach et al. (2020).

REFERENCES

Ardö, J., 2013: A 10-year dataset of basic meteorology and soil properties in central Sudan. *Dataset Pap. Geosci.*, **2013**, 297973, https://doi.org/10.7167/2013/297973.

Armstrong, B., and Coauthors, 2019: The role of humidity in associations of high temperature with mortality: A multicountry, multicity study. *Environ. Health Perspect.*, **127**, 097007, https://doi.org/10.1289/EHP5430.

Azongo, D. K., T. Awine, G. Wak, F. N. Binka, and A. Rexford Oduro, 2012: A time series analysis of weather variables and all-cause mortality in the Kasena-Nankana districts of northern Ghana, 1995–2010. *Global Health Action*, **5**, 19073, https://doi.org/10.3402/gha.v5i0.19073.

Ban, N., J. Rajczak, J. Schmidli, and C. Schär, 2020: Analysis of Alpine precipitation extremes using generalized extreme value theory in convection-resolving climate simulations. *Climate Dyn.*, **55**, 61–75, https://doi.org/10.1007/s00382-018-4339-4.

Barbier, J., F. Guichard, D. Bouniol, F. Couvreux, and R. Roehrig, 2018: Detection of intraseasonal large-scale heat waves: Characteristics and historical trends during the Sahelian spring. *J. Climate*, **31**, 61–80, https://doi.org/10.1175/JCLI-D-17-0244.1.

Berthou, S., E. J. Kendon, D. P. Rowell, M. J. Roberts, S. Tucker, and R. A. Stratton, 2019a: Larger future intensification of rainfall in the West African Sahel in a convection-permitting model. *Geophys. Res. Lett.*, **46**, 13 299–13 307, https://doi.org/10.1029/2019GL083544.

——, D. P. Rowell, E. J. Kendon, M. J. Roberts, R. A. Stratton, J. A. Crook, and C. Wilcox, 2019b: Improved climatological precipitation characteristics over West Africa at convection-permitting scales. *Climate Dyn.*, **53**, 1991–2011, https://doi.org/10.1007/s00382-019-04759-4.

Birch, C. E., J. H. Marsham, D. J. Parker, and C. M. Taylor, 2014a: The scale dependence and structure of convergence fields preceding the initiation of deep convection. *Geophys. Res. Lett.*, **41**, 4769–4776, https://doi.org/10.1002/2014GL060493.

——, D. J. Parker, J. H. Marsham, D. Copsey, and L. Garcia-Carreras, 2014b: A seamless assessment of the role of convection in the water cycle of the West African monsoon. *J. Geophys. Res.*, **119**, 2890–2912, https://doi.org/10.1002/2013JD020887.

Bouniol, D., F. Guichard, J. Barbier, F. Couvreux, and R. Roehrig, 2021: Sahelian heat wave characterization from observational data sets. *J. Geophys. Res. Atmos.*, **126**, e2020JD034465, https://doi.org/10.1029/2020JD034465.

Buzan, J. R., K. Oleson, and M. Huber, 2015: Implementation and comparison of a suite of heat stress metrics within the Community Land Model version 4.5. *Geosci. Model Dev.*, **8**, 151–170, https://doi.org/10.5194/gmd-8-151-2015.

Ceccherini, G., S. Russo, I. Ameztoy, A. F. Marchese, and C. Carmona-Moreno, 2017: Heat waves in Africa 1981–2015, observations and reanalysis. *Nat. Hazards Earth Syst. Sci.*, **17**, 115–125, https://doi.org/10.5194/nhess-17-115-2017.

Chan, S. C., E. J. Kendon, N. M. Roberts, H. J. Fowler, and S. Blenkinsop, 2016: Downturn in scaling of UK extreme rainfall with temperature for future hottest days. *Nat. Geosci.*, **9**, 24–28, https://doi.org/10.1038/ngeo2596.

Coffel, E. D., R. M. Horton, and A. de Sherbinin, 2017: Temperature and humidity based projections of a rapid rise in global heat stress exposure during the 21st century. *Environ. Res. Lett.*, **13**, 014001, https://doi.org/10.1088/1748-9326/aaa00e.

Couvreux, F., and Coauthors, 2015: Representation of daytime moist convection over the semi-arid tropics by parametrizations used in climate and meteorological models. *Quart. J. Roy. Meteor. Soc.*, **141**, 2220–2236, https://doi.org/10.1002/qj.2517.

Crook, J., C. Klein, S. Folwell, C. M. Taylor, D. J. Parker, R. Stratton, and T. Stein, 2019: Assessment of the representation of West African storm lifecycles in convection-permitting simulations. *Earth Space Sci.*, **6**, 818–835, https://doi.org/10.1029/2018EA000491.

Davies-Jones, R., 2008: An efficient and accurate method for computing the wet-bulb temperature along pseudoadiabats. *Mon. Wea. Rev.*, **136**, 2764–2785, https://doi.org/10.1175/2007MWR2224.1.

Diboulo, E., A. Sié, J. Rocklöv, L. Niamba, M. Yé, C. Bagagnan, and R. Sauerborn, 2012: Weather and mortality: A 10 year retrospective analysis of the Nouna Health and Demographic Surveillance System, Burkina Faso. *Global Health Action*, **5**, 19078, https://doi.org/10.3402/gha.v5i0.19078.

Dosio, A., 2017: Projection of temperature and heat waves for Africa with an ensemble of CORDEX regional climate models. *Climate Dyn.*, **49**, 493–519, https://doi.org/10.1007/s00382-016-3355-5.

——, L. Mentaschi, E. M. Fischer, and K. Wyser, 2018: Extreme heat waves under 1.5°C and 2°C global warming. *Environ. Res. Lett.*, **13**, 054006, https://doi.org/10.1088/1748-9326/aab827.

Eyring, V., S. Bony, G. A. Meehl, C. A. Senior, B. Stevens, R. J. Stouffer, and K. E. Taylor, 2016: Overview of the Coupled Model Intercomparison Project phase 6 (CMIP6) experimental design and organization. *Geosci. Model Dev.*, **9**, 1937–1958, https://doi.org/10.5194/gmd-9-1937-2016.

Fiedler, S., and Coauthors, 2020: Simulated tropical precipitation assessed across three major phases of the Coupled Model Intercomparison Project (CMIP). *Mon. Wea. Rev.*, **148**, 3653–3680, https://doi.org/10.1175/MWR-D-19-0404.1.

Finney, D. L., and Coauthors, 2019: Implications of improved representation of convection for the East Africa water budget using a convection-permitting model. *J. Climate*, **32**, 2109–2129, https://doi.org/10.1175/JCLI-D-18-0387.1.

——, J. H. Marsham, D. P. Rowell, E. J. Kendon, S. O. Tucker, R. A. Stratton, and L. S. Jackson, 2020: Effects of explicit convection on future projections of mesoscale circulations, rainfall, and rainfall extremes over eastern Africa. *J. Climate*, **33**, 2701–2718, https://doi.org/10.1175/JCLI-D-19-0328.1.

Fischer, E. M., and R. Knutti, 2013: Robust projections of combined humidity and temperature extremes. *Nat. Climate Change*, **3**, 126–130, https://doi.org/10.1038/nclimate1682.

Fitzpatrick, R. G. J., and Coauthors, 2020a: How a typical West African day in the future-climate compares with current-climate conditions in a convection-permitting and parameterised convection climate model. *Climatic Change*, **163**, 267–296, https://doi.org/10.1007/s10584-020-02881-5.

——, and Coauthors, 2020b: What drives the intensification of mesoscale convective systems over the West African Sahel under climate change? *J. Climate*, **33**, 3151–3172, https://doi.org/10.1175/JCLI-D-19-0380.1.

Fontaine, B., S. Janicot, and P.-A. Monerie, 2013: Recent changes in air temperature, heat waves occurrences, and atmospheric circulation in northern Africa. *J. Geophys. Res.*, **118**, 8536–8552, https://doi.org/10.1002/jgrd.50667.

Gregory, D., and P. R. Rowntree, 1990: A mass flux convection scheme with representation of cloud ensemble characteristics and stability-dependent closure. *Mon. Wea. Rev.*, **118**, 1483–1506, https://doi.org/10.1175/1520-0493(1990)118<1483:AMFCSW>2.0.CO;2.

Guigma, K. H., M. Todd, and Y. Wang, 2020: Characteristics and thermodynamics of Sahelian heatwaves analysed using various thermal indices. *Climate Dyn.*, **55**, 3151–3175, https://doi.org/10.1007/s00382-020-05438-5.

——, F. Guichard, M. Todd, P. Peyrille, and Y. Wang, 2021: Atmospheric tropical modes are important drivers of Sahelian springtime heatwaves. *Climate Dyn.*, **56**, 1967–1987, https://doi.org/10.1007/s00382-020-05569-9.

Gutowski, W. J., Jr., and Coauthors, 2016: WCRP coordinated regional downscaling experiment (CORDEX): A diagnostic MIP for CMIP6. *Geosci. Model Dev.*, **9**, 4087–4095, https://doi.org/10.5194/gmd-9-4087-2016.

Harrington, L. J., and F. E. L. Otto, 2020: Reconciling theory with the reality of African heatwaves. *Nat. Climate Change*, **10**, 796–798, https://doi.org/10.1038/s41558-020-0851-8.

Harris, I., T. J. Osborn, P. Jones, and D. Lister, 2020: Version 4 of the CRU TS monthly high-resolution gridded multivariate climate dataset. *Sci. Data*, **7**, 109, https://doi.org/10.1038/s41597-020-0453-3.

Hart, N. C. G., R. Washington, and R. A. Stratton, 2018: Stronger local overturning in convective-permitting regional climate model improves simulation of the subtropical annual cycle. *Geophys. Res. Lett.*, **45**, 11 334–11 342, https://doi.org/10.1029/2018GL079563.

Hersbach, H., and Coauthors, 2020: The ERA5 global reanalysis. *Quart. J. Roy. Meteor. Soc.*, **146**, 1999–2049, https://doi.org/10.1002/qj.3803.

Hong, J.-S., S.-W. Yeh, and K.-H. Seo, 2018: Diagnosing physical mechanisms leading to pure heat waves versus pure tropical nights over the Korean Peninsula. *J. Geophys. Res. Atmos.*, **123**, 7149–7160, https://doi.org/10.1029/2018JD028360.

Huffman, G., D. Bolvin, D. Braithwaite, K. Hsu, R. Joyce, and P. Xie, 2014: Integrated Multi-satellitE Retrievals for GPM (IMERG), version 6, NASA's Precipitation Processing Center, accessed 23 June 2020, ftp://arthurhou.pps.eosdis.nasa.gov/gpmdata/.

Im, E.-S., J. S. Pal, and E. A. B. Eltahir, 2017: Deadly heat waves projected in the densely populated agricultural regions of South Asia. *Sci. Adv.*, **3**, e1603322, https://doi.org/10.1126/sciadv.1603322.

Jackson, L. S., and Coauthors, 2020: The effect of explicit convection on couplings between rainfall, humidity, and ascent over Africa under climate change. *J. Climate*, **33**, 8315–8337, https://doi.org/10.1175/JCLI-D-19-0322.1.

Kendon, E. J., N. M. Roberts, H. J. Fowler, M. J. Roberts, S. C. Chan, and C. A. Senior, 2014: Heavier summer downpours with climate change revealed by weather forecast resolution model. *Nat. Climate Change*, **4**, 570–576, https://doi.org/10.1038/nclimate2258.

——, R. A. Stratton, S. Tucker, J. H. Marsham, S. Berthou, D. P. Rowell, and C. A. Senior, 2019: Enhanced future changes in wet and dry extremes over Africa at convection-permitting scale. *Nat. Commun.*, **10**, 1794, https://doi.org/10.1038/s41467-019-09776-9.

——, A. F. Prein, C. A. Senior, and A. Stirling, 2021: Challenges and outlook for convection-permitting climate modelling. *Philos. Trans. Roy. Soc.*, **379A**, 20190547, https://doi.org/10.1098/rsta.2019.0547.

Kennedy-Asser, A. T., O. Andrews, D. M. Mitchell, and R. F. Warren, 2020: Evaluating heat extremes in the UK Climate Projections (UKCP18). *Environ. Res. Lett.*, **16**, 014039, https://doi.org/10.1088/1748-9326/abc4ad.

Kjellstrom, T., D. Briggs, C. Freyberg, B. Lemke, M. Otto, and O. Hyatt, 2016: Heat, Human performance, and occupational health: A key issue for the assessment of global climate change impacts. *Ann. Rev. Pub. Health*, **37**, 97–112, https://doi.org/10.1146/annurev-publhealth-032315-021740.

Largeron, Y., F. Guichard, R. Roehrig, F. Couvreux, and J. Barbier, 2020: The April 2010 North African heatwave: When the water vapor greenhouse effect drives nighttime temperatures. *Climate Dyn.*, **54**, 3879–3905, https://doi.org/10.1007/s00382-020-05204-7.

Lebel, T., and Coauthors, 2009: AMMA-CATCH studies in the Sahelian region of West-Africa: An overview. *J. Hydrol.*, **375**, 3–13, https://doi.org/10.1016/j.jhydrol.2009.03.020.

Liao, Z., Y. Chen, W. Li, and P. Zhai, 2021: Growing threats from unprecedented sequential flood-hot extremes across China. *Geophys. Res. Lett.*, **48**, e2021GL094505, https://doi.org/10.1029/2021GL094505.

Lyon, B., 2009: Southern Africa summer drought and heat waves: Observations and coupled model behavior. *J. Climate*, **22**, 6033–6046, https://doi.org/10.1175/2009JCLI3101.1.

Mora, C., and Coauthors, 2017: Global risk of deadly heat. *Nat. Climate Change*, **7**, 501–506, https://doi.org/10.1038/nclimate3322.

Moron, V., B. Oueslati, B. Pohl, S. Rome, and S. Janicot, 2016: Trends of mean temperatures and warm extremes in northern tropical Africa (1961–2014) from observed and PPCA-reconstructed time series. *J. Geophys. Res.*, **121**, 5298–5319, https://doi.org/10.1002/2015JD024303.

Moss, R. H., and Coauthors, 2010: The next generation of scenarios for climate change research and assessment. *Nature*, **463**, 747–756, https://doi.org/10.1038/nature08823.

Oueslati, B., B. Pohl, V. Moron, S. Rome, and S. Janicot, 2017: Characterization of heat waves in the Sahel and associated physical mechanisms. *J. Climate*, **30**, 3095–3115, https://doi.org/10.1175/JCLI-D-16-0432.1.

Pal, J. S., and E. A. B. Eltahir, 2016: Future temperature in southwest Asia projected to exceed a threshold for human adaptability. *Nat. Climate Change*, **6**, 197–200, https://doi.org/10.1038/nclimate2833.

Pastorello, G., and Coauthors, 2020: The FLUXNET2015 dataset and the ONEFlux processing pipeline for eddy covariance data. *Sci. Data*, **7**, 225, https://doi.org/10.1038/s41597-020-0534-3.

Perkins-Kirkpatrick, S. E., and S. C. Lewis, 2020: Increasing trends in regional heatwaves. *Nat. Commun.*, **11**, 3357, https://doi.org/10.1038/s41467-020-16970-7.

Prein, A. F., and Coauthors, 2015: A review on regional convection-permitting climate modeling: Demonstrations, prospects, and challenges. *Rev. Geophys.*, **53**, 323–361, https://doi.org/10.1002/2014RG000475.

Raghavendra, A., A. Dai, S. M. Milrad, and S. R. Cloutier-Bisbee, 2019: Floridian heatwaves and extreme precipitation: Future climate projections. *Climate Dyn.*, **52**, 495–508, https://doi.org/10.1007/s00382-018-4148-9.

Raymond, C., and Coauthors, 2021: On the controlling factors for globally extreme humid heat. *Geophys. Res. Lett.*, **48**, e2021GL096082, https://doi.org/10.1029/2021GL096082.

Reynolds, R. W., T. M. Smith, C. Liu, D. B. Chelton, K. S. Casey, and M. G. Schlax, 2007: Daily high-resolution-blended analyses for sea surface temperature. *J. Climate*, **20**, 5473–5496, https://doi.org/10.1175/2007JCLI1824.1.

Rohde, R. A., and Z. Hausfather, 2020: The Berkeley Earth Land/Ocean temperature record. *Earth Syst. Sci. Data*, **12**, 3469–3479, https://doi.org/10.5194/essd-12-3469-2020.

Russo, S., J. Sillmann, and E. M. Fischer, 2015: Top ten European heatwaves since 1950 and their occurrence in the coming decades. *Environ. Res. Lett.*, **10**, 124003, https://doi.org/10.1088/1748-9326/10/12/124003.

——, A. F. Marchese, J. Sillmann, and G. Immé, 2016: When will unusual heat waves become normal in a warming Africa? *Environ. Res. Lett.*, **11**, 054016, https://doi.org/10.1088/1748-9326/11/5/054016.

——, J. Sillmann, and A. Sterl, 2017: Humid heat waves at different warming levels. *Sci. Rep.*, **7**, 7477, https://doi.org/10.1038/s41598-017-07536-7.

Seneviratne, S. I., and Coauthors, 2021: Weather and climate extreme events in a changing climate. *Climate Change 2021: The Physical Science Basis*, V. Masson-Delmotte et al., Eds., Cambridge University Press, 1513–1766, https://doi.org/10.1017/9781009157896.013.

Senior, C. A., 2019a: P25-Present: Present-day 25km regional pan-Africa data. Centre for Environmental Data Analysis, accessed November 2019, https://catalogue.ceda.ac.uk/uuid/4e362effa16146abbe45c2c58f1e54ed.

——, 2019b: CP4A-Present: Present-day climate predictions for Africa, Centre for Environmental Data Analysis, accessed November 2019, https://catalogue.ceda.ac.uk/uuid/f46b14e670fc49cbaadf108c969e7ee0.

——, 2019c: P25-Future: Future 25km regional pan-Africa data. Centre for Environmental Data Analysis, accessed November 2019, https://catalogue.ceda.ac.uk/uuid/8f8eab18b07e420a9b7230d86ed172fe.

——, 2019d: CP4A-Future: Future climate predictions for Africa. Centre for Environmental Data Analysis, accessed November 2019, https://catalogue.ceda.ac.uk/uuid/a027093520b2432b8e782e3edefd6b47.

——, and Coauthors, 2021: Convection permitting regional climate change simulations for understanding future climate and informing decision making in Africa. *Bull. Amer. Meteor. Soc.*, **102**, E1206–E1223, https://doi.org/10.1175/BAMS-D-20-0020.1.

Sherwood, S. C., 2018: How important is humidity in heat stress? *J. Geophys. Res.*, **123**, 11 808–11 810, https://doi.org/10.1029/2018JD028969.

——, and M. Huber, 2010: An adaptability limit to climate change due to heat stress. *Proc. Natl. Acad. Sci. USA*, **107**, 9552–9555, https://doi.org/10.1073/pnas.0913352107.

Stratton, R. A., and Coauthors, 2018: A pan-African convection-permitting regional climate simulation with the Met Office Unified Model: CP4-Africa. *J. Climate*, **31**, 3485–3508, https://doi.org/10.1175/JCLI-D-17-0503.1.

Taylor, C. M., C. E. Birch, D. J. Parker, N. Dixon, F. Guichard, G. Nikulin, and G. M. S. Lister, 2013: Modeling soil moisture–precipitation feedback in the Sahel: Importance of spatial scale versus convective parameterization. *Geophys. Res. Lett.*, **40**, 6213–6218, https://doi.org/10.1002/2013GL058511.

Taylor, K. E., R. J. Stouffer, and G. A. Meehl, 2012: An overview of CMIP5 and the experiment design. *Bull. Amer. Meteor. Soc.*, **93**, 485–498, https://doi.org/10.1175/BAMS-D-11-00094.1.

Tölle, M. H., L. Schefczyk, and O. Gutjahr, 2018: Scale dependency of regional climate modeling of current and future climate extremes in Germany. *Theor. Appl. Climatol.*, **134**, 829–848, https://doi.org/10.1007/s00704-017-2303-6.

Vicedo-Cabrera, A. M., and Coauthors, 2021: The burden of heat-related mortality attributable to recent human-induced climate change. *Nat. Climate Change*, **11**, 492–500, https://doi.org/10.1038/s41558-021-01058-x.

Walters, D., and Coauthors, 2017: The Met Office Unified Model global atmosphere 6.0/6.1 and JULES global land 6.0/6.1 configurations. *Geosci. Model Dev.*, **10**, 1487–1520, https://doi.org/10.5194/gmd-10-1487-2017.

You, J., and S. Wang, 2021: Higher probability of occurrence of hotter and shorter heat waves followed by heavy rainfall. *Geophys. Res. Lett.*, **48**, e2021GL094831, https://doi.org/10.1029/2021GL094831.

Zhang, W., and G. Villarini, 2020: Deadly compound heat stress-flooding hazard across the central United States, *Geophys. Res. Lett.*, **47**, e2020GL089185, https://doi.org/10.1029/2020GL089185.

Zhao, Y., A. Ducharne, B. Sultan, P. Braconnot, and R. Vautard, 2015: Estimating heat stress from climate-based indicators: Present-day biases and future spreads in the CMIP5 global climate model ensemble. *Environ. Res. Lett.*, **10**, 084013, https://doi.org/10.1088/1748-9326/10/8/084013.